Time-dependent brittle creep in Darley Dale sandstone

Citation for published version:
Heap, MJ, Baud, P, Meredith, PG, Bell, AF & Main, IG 2009, 'Time-dependent brittle creep in Darley Dale sandstone', *Journal of Geophysical Research*, vol. 114, no. B7, B07203.
https://doi.org/10.1029/2008JB006212

Digital Object Identifier (DOI):
10.1029/2008JB006212

Link:
Link to publication record in Edinburgh Research Explorer

Document Version:
Publisher's PDF, also known as Version of record

Published In:
Journal of Geophysical Research

JOURNAL OF GEOPHYSICAL RESEARCH, VOL. 114, B07203, doi:10.1029/2008JB006212, 2009

Time-dependent brittle creep in Darley Dale sandstone

M. J. Heap,[1] P. Baud,[2] P. G. Meredith,[1] A. F. Bell,[3] and I. G. Main[3]

Received 12 November 2008; revised 16 April 2009; accepted 1 June 2009; published 11 July 2009.

[1] The characterization of time-dependent brittle rock deformation is fundamental to understanding the long-term evolution and dynamics of the Earth's crust. The chemical influence of pore water promotes time-dependent deformation through stress corrosion cracking that allows rocks to deform at stresses far below their short-term failure strength. Here, we report results from a study of time-dependent brittle creep in water-saturated samples of Darley Dale sandstone (initial porosity, 13%) under triaxial stress conditions. Results from conventional creep experiments show that axial strain rate is heavily dependent on the applied differential stress. A reduction of only 10% in differential stress results in a decrease in strain rate of more than two orders of magnitude. However, natural sample variability means that multiple experiments must be performed to yield consistent results. Hence we also demonstrate that the use of stress-stepping creep experiments can successfully overcome this issue. We have used the stress-stepping technique to investigate the influence of confining pressure at effective confining pressures of 10, 30, and 50 MPa (while maintaining a constant 20 MPa pore fluid pressure). Our results demonstrate that the stress corrosion process appears to be significantly inhibited at higher effective pressures, with the creep strain rate reduced by multiple orders of magnitude. The influence of doubling the pore fluid pressure, however, while maintaining a constant effective confining pressure, is shown to influence the rate of stress corrosion within the range expected from sample variability. We discuss these results in the context of microstructural analysis, acoustic emission hypocenter locations, and fits to proposed macroscopic creep laws.

Citation: Heap, M. J., P. Baud, P. G. Meredith, A. F. Bell, and I. G. Main (2009), Time-dependent brittle creep in Darley Dale sandstone, *J. Geophys. Res.*, *114*, B07203, doi:10.1029/2008JB006212.

1. Introduction

[2] The majority of rocks forming the Earth's crust, even those at depth, contain microporosity comprising some or all of open pores between grains, triple-junction voids between crystalline phases, grain boundary voids and open microcracks. Water and aqueous solutions are ubiquitous in the upper crust, and below a few hundred meters these void spaces in most rocks are saturated. The presence of a fluid phase not only affects the mechanical behavior of rock, but also allows chemical rock-fluid interactions to occur. In a purely mechanical sense, a pressurized pore fluid acts to reduce all the applied normal stresses and thus allows rocks to fail at lower applied differential stress (Q) than would otherwise be the case [*Terzaghi*, 1943; *Jaeger et al.*, 2007]. Chemically, aqueous solutions affect the deformation of rock in two main ways: (1) they act to weaken the rock via the reduction of surface free energy as the result of the absorption of pore fluid onto the internal pore surfaces [*Orowan*, 1944; *Rehbinder*, 1948; *Andrade and Randall*, 1949], and (2) they also weaken rocks by promoting subcritical crack growth, of which stress corrosion is considered the most important mechanism under upper crustal conditions [*Anderson and Grew*, 1977; *Atkinson*, 1984; *Atkinson and Meredith*, 1987; *Costin*, 1987].

[3] Stress corrosion describes the reactions that occur preferentially between a chemically active pore fluid, most commonly water, and the strained atomic bonds close to crack tips. In a silicate-water system, bridging bonds close to crack tips, the main stress-supporting components, are replaced by weaker hydrogen bonds, thus facilitating crack growth at lower levels of stress than would otherwise be the case [*Michalske and Freiman*, 1982, 1983; *Freiman*, 1984; *Hadizadeh and Law*, 1991]. The velocity of cracks propagating by stress corrosion has been shown to increase when the stress intensity (a function of the applied stress and the crack length) at the crack tip is increased in a wide variety of rock types (see *Atkinson* [1984] and *Atkinson and Meredith* [1987] for reviews). However, the majority of experimental data on stress corrosion cracking has been derived from experiments on single cracks at ambient pressure, and few data exist on the bulk behavior of rock containing a population of cracks. Nevertheless, it has been hypothesized that, for bulk rock deforming in a brittle manner under triaxial stress conditions, stress corrosion will

---

[1] Rock and Ice Physics Laboratory, Department of Earth Sciences, University College London, London, UK.

[2] EOST, CNRS/ULP, Strasbourg, France.

[3] School of GeoSciences, University of Edinburgh, Grant Institute, Edinburgh, UK.

0148-0227/09/2008JB006212$09.00

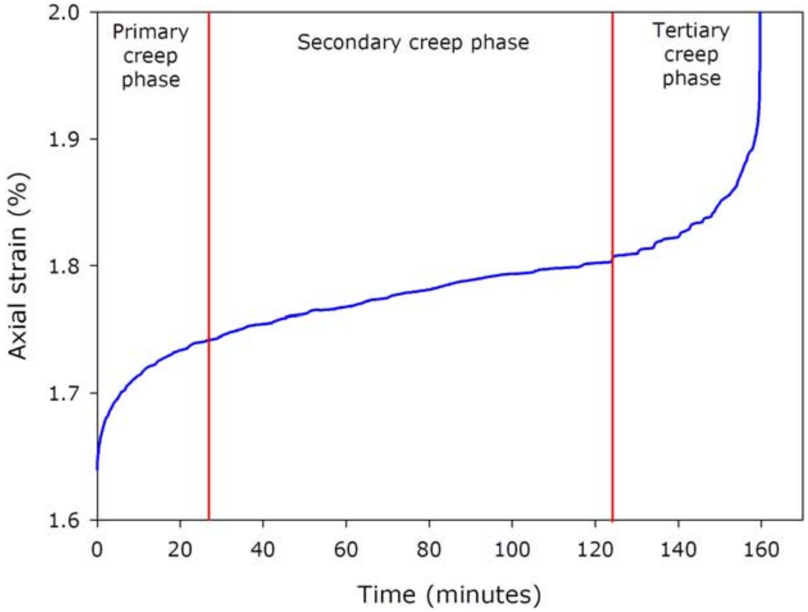

Figure 1. The classic trimodal creep curve for brittle material at a constant applied differential stress. The curve shows the three stages of brittle creep: (1) primary or decelerating, (2) secondary or "steady state," and (3) tertiary or accelerating creep. The linear "steady state" portion is where creep strain rates are calculated. Data are from experiment DD-40-45Z.

lead to highly nonlinear time-dependent deformation [*Main et al.*, 1993; *Main*, 2000]. This allows rocks to deform even under a constant Q over extended periods of time; a phenomenon known as *brittle creep* (or *static fatigue* in the engineering literature). This style of deformation has conventionally been described as exhibiting an apparent trimodal behavior when axial strain is plotted against time (commonly known as a *creep curve*). The three stages of the creep curve have conventionally been described as; (1) primary or decelerating creep, (2) secondary or steady state creep, and (3) tertiary or accelerating creep (as illustrated in Figure 1). There have been relatively few studies of brittle creep in sandstone [*Lockner and Byerlee*, 1975; *Rutter and Mainprice*, 1978; *Baud and Meredith*, 1997; *Ngwenya et al.*, 2001; *Ojala et al.*, 2003], but they all report that the level of Q exerts a crucial influence on the strain rate during secondary creep and, hence, on the overall time-to-failure. *Ngwenya et al.* [2001] investigated brittle creep in four reservoir sandstones with contrasting petrophysical properties (e.g., porosities ranging from 4% to 35%) and found that creep deformation had a different sensitivity to the level of Q, depending on the initial state of damage (represented by the porosity). *Baud and Meredith* [1997] measured axial strain, pore volume change and the output of acoustic emission (AE) energy as proxies for crack damage, and reported that the values of all three proxies were approximately equal at the onset of tertiary creep, regardless of the level of applied stress and the time taken to reach that point. They suggested that the onset of tertiary creep marked the transition from the stable growth of isolated cracks to unstable crack interaction and coalescence, and that this occurs at a critical level of damage.

[4] Time-dependent brittle deformation is a fundamental and pervasive process in the Earth's brittle upper crust. Hence the characterization of time-dependent processes is a critical prerequisite for understanding its long-term behavior and strength. Furthermore, the process of stress corrosion is the mechanism considered most likely to be responsible for the time-dependent precursory cracking, displacement and accelerating seismic activity that commonly precedes earthquake rupture [*Scholz*, 1968a; *Das and Scholz*, 1981; *Crampin et al.*, 1984; *Main and Meredith*, 1991; *Main et al.*, 1992] and volcanic eruptions [*Voight*, 1988, 1989; *Cornelius and Scott*, 1993; *McGuire and Kilburn*, 1997; *Kilburn and Voight*, 1998; *Main*, 1999; *Kilburn*, 2003]. Stress corrosion cracking in rock has also been used to explain the growth and development of joints [*Olson*, 1993; *Renshaw and Pollard*, 1994; *Savalli and Engelder*, 2005] and is important when assessing the instability potential of underground excavations [*Diederichs and Kaiser*, 1999].

[5] Here we report results from a systematic experimental study of brittle creep in Darley Dale sandstone under triaxial stress conditions. We first describe the study material and explain the experimental techniques. We then present benchmark results from a series of constant strain rate experiments and conventional brittle creep experiments. This is followed by results from stress-stepping experiments in which the influences of effective confining pressure (Peff) and pore fluid pressure (Pp) on brittle creep were investigated. Finally, we show the results of fitting macroscopic creep laws based on damage mechanics to our experimental data.

2. Sample Material and Preparation

[6] The material used throughout this study was Darley Dale sandstone (Derbyshire, England). Darley Dale sandstone (DDS) is a brown-yellow, well-indurated, feldspathic

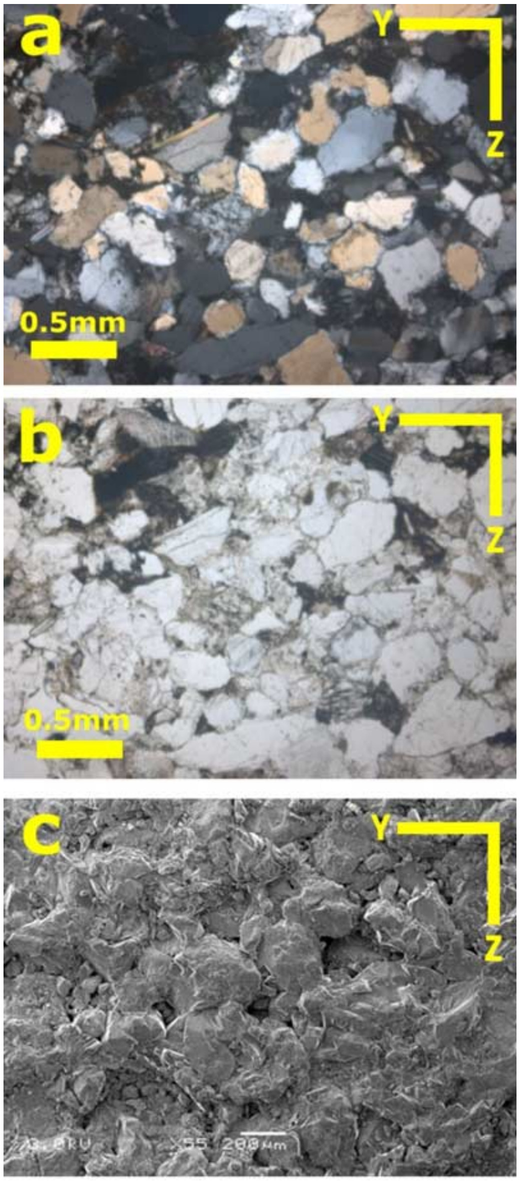

Figure 2. Pictures of Darley Dale sandstone: (a) photomicrograph under cross-polarized light, (b) photomicrograph under plane-polarized light, and (c) uncoated scanning electron microscope picture at ×55 magnification. *Z* axis is normal to the axial loading direction.

sandstone with a connected porosity of 13.3 ± 0.8%. The modal composition is 69% quartz, 26% feldspar, 3% clay and 2% mica. Optical microscopy and SEM analyses have demonstrated that the grains are subangular, vary in size from 100–800 μm and show no discernable preferred alignment (Figure 2). No distinct layering or lamination is observed in hand specimen, but benchtop ultrasonic wave velocity measurements indicate a P wave velocity anisotropy of about 6.5%. During our experiments we do not expect any significant Pp gradient due to the high permeability of DDS of 5×10^{-15} m^2 at the implemented experimental pressure conditions [*Zhu and Wong*, 1997]. The modal composition and physical properties of DDS are summarized in Table 1. All samples were cored perpendicular to bedding from the same block of material to a diameter of 40 mm. They were precision-ground to 100 ± 0.02 mm in length, resulting in a length:diameter ratio of 2.5:1 [*Mogi*, 1966; *Hawkes and Mellor*, 1970]. Samples were then vacuum-saturated in distilled water for 24 hours prior to experimentation.

3. Experimental Methodology

[7] All experiments were performed at room temperature in a servo-controlled 400 MPa triaxial rock deformation apparatus in the Rock & Ice Physics Laboratory (RIPL) at University College London. Samples were mounted between two steel end-caps within a nitrile rubber sleeve containing inserts for the mounting of acoustic emission transducers. The sample assembly is shown in Figure 3a. During all experiments, axial strain was measured continuously using LVDT displacement transducers, and pore volume change was measured continuously using a servo-controlled pore fluid pressure intensifier and volumometer [*Benson et al.*, 2007]. A constant confining pressure (Pc) was achieved using silicone oil fed from a large-volume hydraulic pump coupled to a servo-controlled pressure intensifier. Acoustic emission (AE) output was recorded continuously via ten PZT-5A transducers (3 mm in diameter and 1 MHz longitudinal resonant frequency) mounted on steel inserts embedded within the nitrile sample jacket, and stored by a Vallen AMSY-5 acoustic emission acquisition system. The relative positions of the ten AE recording transducers are shown in Figure 3b. AE hypocenters were located in three-dimensional for selected experiments, with a location accuracy of ±2 mm, using the methodology described by *Townend et al.* [2008].

[8] Prior to performing brittle creep experiments, a series of constant strain rate tests were conducted at a strain rate of 1.0×10^{-5} s^{-1} and a Peff of 30 MPa (Pc of 50 MPa and Pp of 20 MPa) in order to establish the short-term failure characteristics of the test material. Once this had been established, a series of conventional brittle creep experiments were performed under the same effective stress conditions. In these latter experiments, samples of DDS were first loaded to a predetermined percentage of the short-term peak stress (σ_p) established during the constant strain rate experiments. Generally, this was in the range 80 to 90% of the short-term strength (see also *Baud and Meredith*, 1997). Following this preloading, samples were allowed to deform under constant Q until failure. The evolution of crack damage was monitored throughout each experiment

Table 1. Modal Composition and Physical Properties of the Darley Dale Sandstone Used Throughout This Study[a]

Modal composition	69% quartz, 26% feldspar, 3% clay and 2% mica
Porosity (connected)	13.3 ± 0.8%
Grain size	100–800 μm
Peak stress (σ_p) (Pc = 50 MPa; Pc = 20 MPa)	155 ± 6 MPa
Mean P wave velocity	3.32 km s^{-1} (dry) and 3.60 km s^{-1} (wet)
Mean S wave velocity	2.23 km s^{-1}

[a] Abbreviations: Pc, confining pressure; Pp, pore fluid pressure.

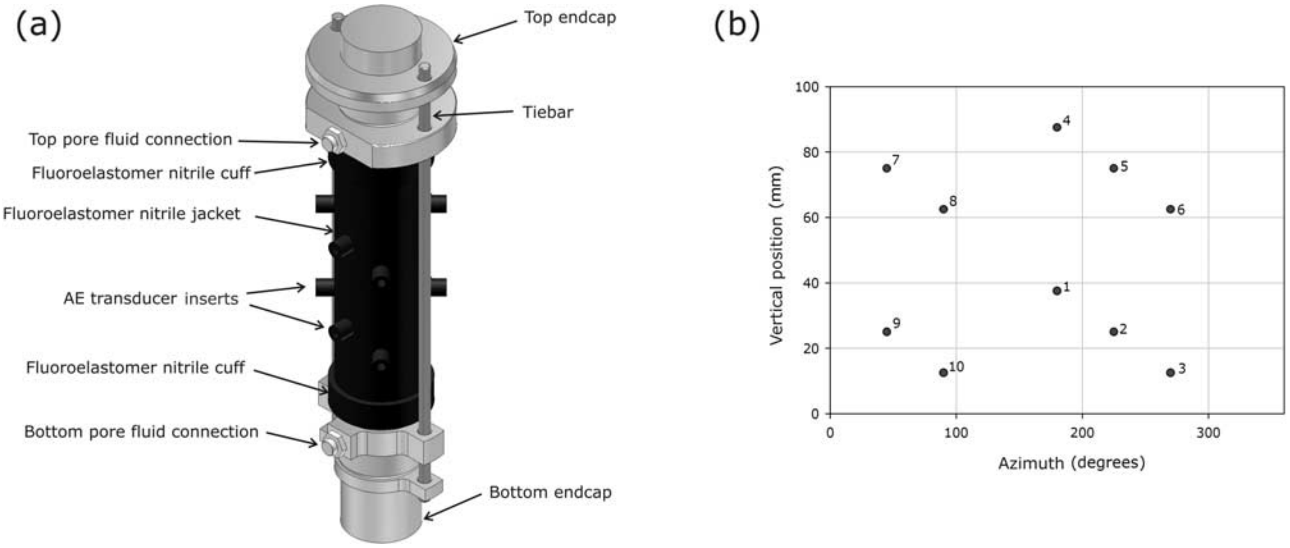

Figure 3. (a) Three-dimensional Autodesk Inventor picture of the jacketed sample setup. (b) Angular position of the 10 piezoelectric transducers located on steel inserts within the sample jacket. *Z* axis is normal to the axial loading direction.

by measuring the damage proxies of axial strain, pore volume change and output of AE energy. At the end of each experiment, creep strain rates were calculated from the linear portion within the secondary phase of the creep curve (see Figure 1).

[9] A number of focused experiments were performed to investigate the spatial distribution and density of cracking at the onset of tertiary creep. During these experiments, samples of DDS were allowed to deform to the onset of tertiary creep at different but constant values of Q that produced different creep strain rates. Once deformation reached the onset of tertiary creep, the samples were slowly unloaded; and the Pc and Pp decreased to ambient values. Samples were then removed from the apparatus, and epoxy-impregnated thin sections were prepared for microscopic analysis. Crack densities were determined using the same method as that reported by *Wu et al.* [2000] for measurements on DDS [see also, *Underwood*, 1970]. Linear crack densities and orientations were measured over a gridded area of 11 × 11 mm^2 from the same relative location within each sample. This was achieved by counting the number of crack intersections (P) with grid lines (at 0.1 mm spacing) orientated both normal ($P_\perp$) and parallel ($P_\parallel$) to the axial loading direction.

[10] A key aspect of any study involving experiment over extended periods of time is the stability of measurements over the maximum experiment duration. The stability of our experimental system was therefore determined by loading a sample of DDS to a low percentage (60%) of the short-term strength and holding this stress constant for ten days. During this period, the servo-controlled parameters of axial load, Pc and Pp all remained essentially constant, and fluctuations in the axial strain and pore volume change were both less than 0.1%. The maximum diurnal range in ambient laboratory temperature was ±2.5°C, but this reduced to ±0.3°C inside the deformation cell, most likely due to the large thermal mass of the cell (approx. 1100 kg of nickel chrome alloy steel). This small temperature fluctuation did not significantly affect any of the other measured parameters.

4. Results

4.1. Constant Strain Rate Experiments

[11] As noted above, a series of constant strain rate experiments were first undertaken on samples of DDS in order to establish its short-term deformation and failure characteristics. A key goal was to ascertain the reproducibility of σ_p that would be used to guide the applied stress in later creep tests. Figure 4 shows the stress-strain curves and the variation in pore volume and cumulative AE energy for two representative experiments conducted at a constant strain rate of 1.0×10^{-5} s^{-1} and a Peff of 30 MPa. The repeatability is excellent, and the small variation between the two sets of curves simply reflects the variability between rock samples. A series of experiments yielded a mean σ_p of 155 ± 6 MPa. Following an initial period of compaction, the onset of dilatancy, termed C' [*Wong et al.*, 1997], occurs at a Q of around 40 MPa and is marked on the Q versus volumetric strain curve presented as Figure 5. As expected, this also corresponds to the onset of AE output around 0.5% axial strain as shown in Figure 4c. The minimum in the pore volume change curve (Figure 4b) marks the transition from compaction-dominated deformation to dilatancy-dominated deformation, which we term D'. This also corresponds to the maximum in the volumetric strain (Figure 5), and occurs at a Q of around 130 MPa.

[12] Figure 6 shows the results from a series of experiments to investigate the influence of Peff on the deformation of DDS at a constant strain rate of 1.0×10^{-5} s^{-1}. Increasing the Peff results in significant increases in the σ_p, the duration of the strain softening phase that precedes failure and the axial strain at dynamic failure (Figure 6a). Similar observations in sandstone have been reported by

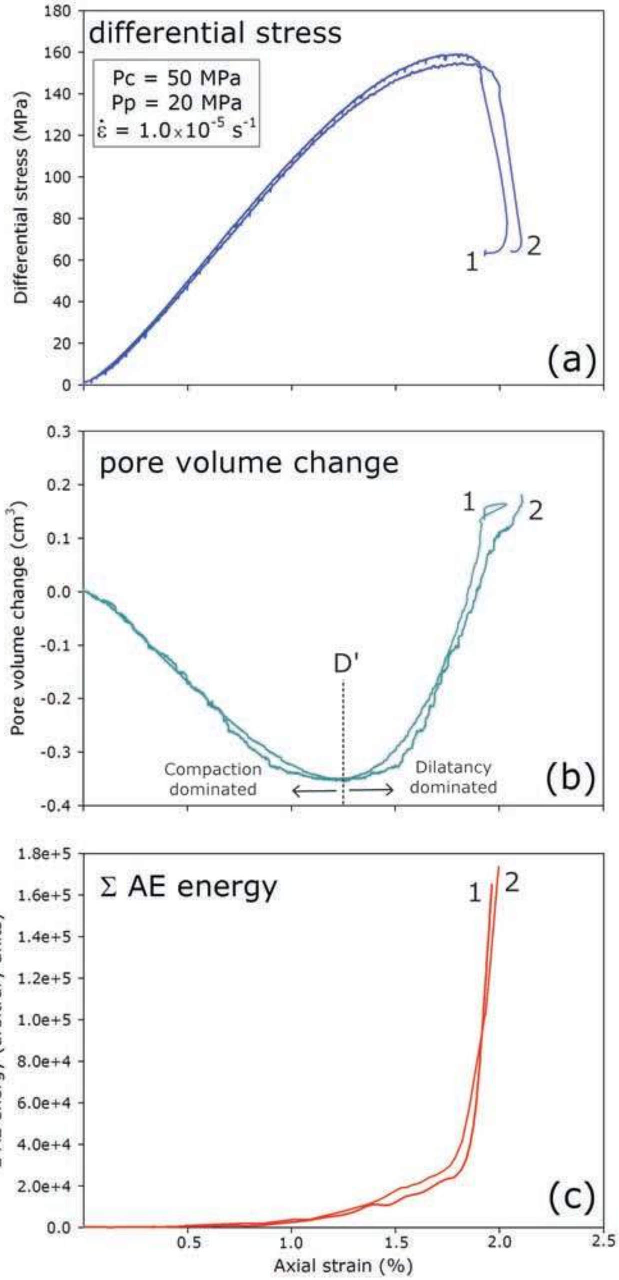

Figure 4. Two conventional constant strain rate experiments on water-saturated DDS showing variability in the three proxies for damage within the rock: (a) stress-strain curves, (b) pore volume change curves, and (c) AE energy output curves. Experimental conditions are indicated. *D*′, the stress at which a dilatant-dominated regime dominates, is indicated in Figure 4b. Pc, confining pressure; Pp, pore fluid pressure.

[*Wong et al.*, 1997; *Baud et al.*, 2000]. Figure 6b also shows pore volume variation is also strongly influenced by the Peff. Indeed, the axial strain at which *D*′ occurs increases significantly. Since the transition from compaction to dilatancy occurs later with increasing Peff, it is perhaps not surprising that the onset of significant AE output (Figure 6c) also occurs later. However, we note that the total output of AE energy does not vary significantly between experiments even though the rock strength increases by over 70%, from 105 MPa to 182 MPa.

4.2. Conventional Brittle Creep Experiments

[13] Conventional creep experiments were performed on samples of DDS over a range of constant values of Q in order to yield times-to-failure and creep strain rates over several orders of magnitude. Following *Baud and Meredith* [1997], the levels of Q were selected to be greater than that corresponding to the onset of dilatancy (*C*′), but lower than the stress level that would generate very rapid failure within a few seconds or a few minutes. Such stress levels generally corresponded to between 80% and 90% of the σ_p in short-term constant strain rate experiments (Figure 4). Figure 7 shows the results from three such experiments conducted across this applied stress range. The three independent proxy measures of damage (axial strain, pore volume change and cumulative AE energy) are shown plotted against time for each experiment.

[14] All of the axial strain curves show the trimodal behavior via which creep deformation has generally been interpreted [Figure 1, see also *Baud and Meredith*, 1997; *Main*, 2000, among others]. Each primary creep phase is characterized by an initially high strain rate that decreases with time to reach a quasilinear secondary phase that is often interpreted as steady state creep. After an extended period of time, a tertiary phase is entered, characterized by accelerating strain. This eventually results in macroscopic failure of the samples by propagation of a shear fault. Creep strain rates were calculated for each experiment from the linear portions of the strain-time curves. Linear behavior was confirmed by plotting the first derivatives of the strain-time curves (i.e. strain rates against time); an example of one such plot is shown in Figure 8. The plot demonstrates that there is a large constant strain rate portion of the curve as evidenced by the plateau in the strain rate i.e. there is a real steady state creep phase. The steady state creep strain rate was subsequently calculated within this portion of the creep curve. Our data show that both the creep strain rate and the overall time-to-failure depend strongly and non-linearly on the level of Q. Even modest increases in applied stress can result in order of magnitude changes in times-to-failure and creep strain rates. At 141 MPa (90% of σ_p), the time-to-failure was approximately 10 minutes and the creep strain rate was $3.6 \times 10^{-6}\ s^{-1}$. At 132 MPa (85% of σ_p), the time-to-failure increased to 160 minutes and the creep strain rate decreased to $1.0 \times 10^{-7}\ s^{-1}$. Finally, for 125 MPa (80% of σ_p), the time-to-failure was 3600 minutes and the creep strain rate was $1.3 \times 10^{-8}\ s^{-1}$. In summary, a 10% reduction in Q resulted in an increase in time-to-failure and a decrease in creep strain rate of approximately 2.5 orders of magnitude.

[15] The two other damage proxies of pore volume change and cumulative AE energy also exhibit trimodal behavior throughout, although the curves are visibly less smooth in some cases. This is particularly the case for the pore volume change and cumulative AE curves at the lowest Q (125 MPa; Figures 7f and 7i). In this case, there is a much greater contribution to the total pore volume change and cumulative AE energy during the primary creep phase than for the experiments at higher applied stresses. In

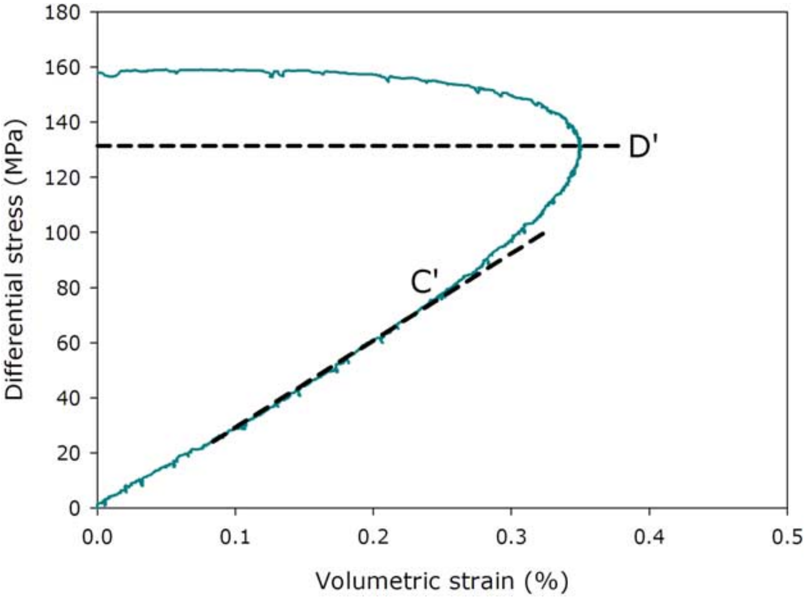

Figure 5. Volumetric strain against differential stress for a constant strain rate experiment on water-saturated DDS. Both *C*′, the stress at which the volumetric strain deviates from that observed from hydrostatic loading (elastic deformation), and *D*′, the stress at which a dilatant-dominated regime dominates, are indicated.

fact, the pore volume appears to remain essentially constant during the whole of the secondary creep phase.

[16] In all cases, the tertiary creep phase is characterized by accelerations in all three proxies for damage. Furthermore, the value of each of the three proxy measures at the onset of tertiary creep is in a very narrow range, regardless of the different applied stresses and the very different lengths of time required to reach that point; an axial strain in the range of 1.80 to 1.88%, a pore volume change in the range -0.15 to 0.01 cm^3, and cumulative AE energy in the range of 10^4 units. This implies that the onset of tertiary creep occurs at a similar level of crack damage in all cases.

[17] Results from the two creep experiments that were stopped at the onset of tertiary creep in order to investigate the spatial distribution and density of microcracking are shown in Figure 9. These experiments were conducted at a Q of 137 MPa and 131 MPa, resulting in creep strain rates of 1.4×10^{-6} s^{-1} and 1.7×10^{-7} s^{-1}, respectively. The linear crack densities from these two samples, together with those from an undeformed sample and a sample taken to failure (but measured away from the localized shear band) for comparison, are displayed in Table 2, together with their anisotropies. Figure 10 shows photomicrographs of the two samples taken to the onset of tertiary creep (Figures 10a and 10b), together with the shear band in the postfailure sample (Figure 10c) and microcracking in the failed sample (Figure 10d). A micrograph of an undeformed sample, at the same scale, can be seen in Figure 2. The results of the microstructural analysis (Table 2) show that the linear crack densities ($P_\perp$ and $P_\parallel$) and the crack area per unit volume all increase from the values for the undeformed state for both samples taken to the onset of tertiary creep, and increase markedly more for the sample taken to failure. While the increases for the samples taken to the onset of tertiary creep are modest (11 to 44%), the increase for the sample taken to failure is much greater (300 to 700%). This can also be clearly seen in the photomicrographs of Figure 10. Similar trends are seen in the crack anisotropy, with the crack fabric for the sample taken to failure dominated by axial microcracks.

[18] The relation between Q and creep strain rate (calculated from the linear portions of the trimodal creep curves) is shown in Figure 11. The relation is nonlinear and very stress sensitive, and is therefore plotted on semilog axes. This stress sensitivity means that any variations in the initial state of damage (e.g., porosity or crack density) of test samples is likely to produce large variations in their creep behavior, even when deformed under identical conditions. In turn, this is likely to be a significant problem when using natural materials such as porous rocks, because there is inevitably variation in porosity and crack density between different samples even when cored from the same block of material. We attempted to overcome this problem by measuring the porosity, bulk density and elastic wave velocities of all our samples prior to testing, and rejecting samples where these measures fell outside a very narrow range. This inevitably led to considerable sample wastage. However, the consequence of not pursuing such a rigorous approach is illustrated by the solid square in Figure 11, which shows data for a sample with a marginally higher porosity and lower bulk density than our main suite of samples. This resulted in a strain rate that was several orders of magnitude higher than that achieved at the same level of stress for our carefully preselected samples. The same problem has previously been reported by *Baud and Meredith* [1997]. In order to circumvent this problem of sample variability, we adopted the methodology of stress-stepping in which mul-

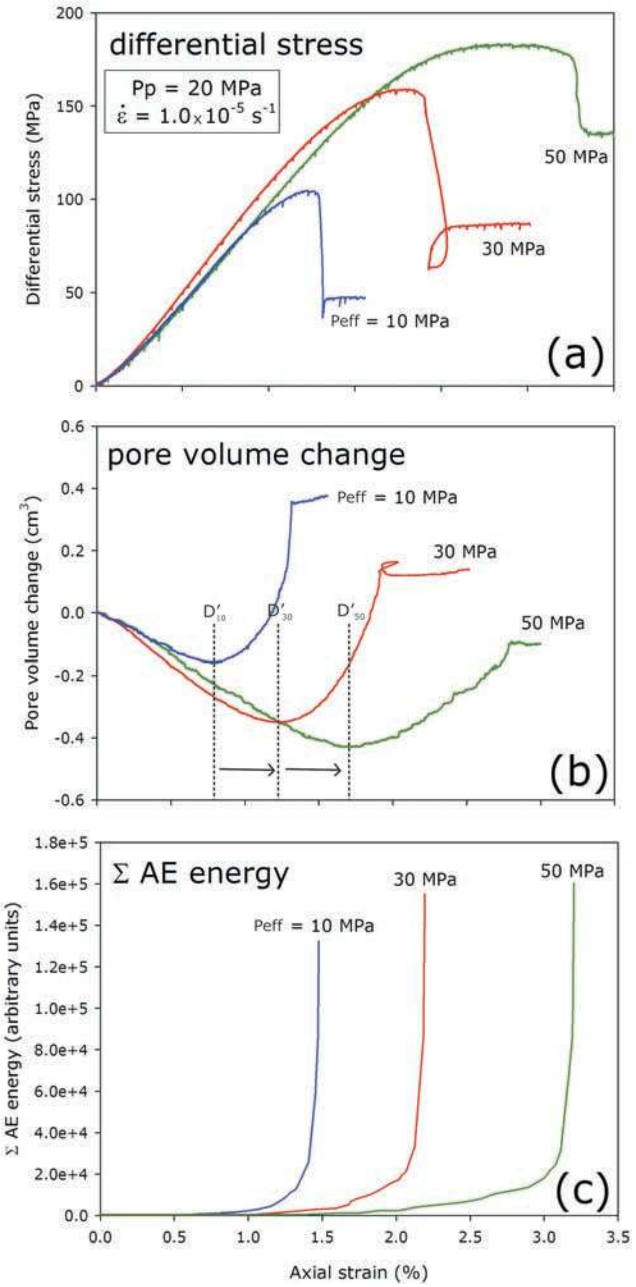

Figure 6. Conventional constant strain rate experiments on water-saturated DDS showing variability in (a) the stress-strain curves, (b) the pore volume change curves, and (c) the AE energy output curves for effective confining pressures of 10, 30, and 50 MPa while maintaining a constant pore fluid pressure of 20 MPa. Experimental conditions are indicated. The position of D', as well as how it migrates with increasing effective confining pressure, is indicated in Figure 6b. Pp, pore fluid pressure; Peff, effective confining pressure.

tiple brittle creep experiments can be conducted on a single sample.

4.3. Stress-Stepping Brittle Creep Experiments

[19] The overall aim of using the stress-stepping methodology is to be able to capture the type of data shown in Figure 11 using a single sample, so that we can be confident that the problem of sample variability is eliminated. In turn, this would allow us to quantify the effect of other experimental variables of interest in a more sample and time efficient manner. The stress-stepping approach has previously been used and has shown to provide reliable data [*Lockner*, 1993a; *Maranini and Brignoli*, 1999; *Ngwenya et al.*, 2001, among others].

[20] A key point before starting any stress-stepping creep experiments is to determine the level of Q to be applied in the first stress step. Since the exact σ_p of any particular sample cannot be known prior to the experiment due to sample variability, we cannot use a predetermined percentage of the unknown σ_p, as explained at the end of the previous section. It is also clear that the sample will not creep at stress levels within the elastic regime; that is, below that required for the onset of dilatant cracking (C'). However, while C' can be determined relatively easily from the volumetric strain curve after an experiment, it is not easily determined in real time during an experiment. We have therefore chosen to use D' (the transition from compaction-dominated deformation to dilatancy-dominated deformation as seen on pore volume change curves) as the starting point for our stress-stepping experiments. This has several advantages: (1) it is relatively easy to determine in real time during experiments because it is a minimum, (2) it is likely to represent a reproducible state of damage within the material and (3) because it marks the onset of dilatancy dominated deformation, it is likely to induce a creep strain rate that is sufficiently high to be relatively easily measured. Therefore during stress-stepping experiments, samples were first loaded at a constant strain rate of 1.0×10^{-5} s^{-1} to D' (monitored from the pore volume change curve and regardless of the level of applied stress required to reach this point). At this point, the loading was stopped and the sample allowed to deform through primary creep and into secondary creep at constant Q. Once the sample had undergone approximately 0.15 mm of axial shortening (equivalent to 0.15% axial strain) during secondary creep, the stress was stepped up by a small increment (usually in the range 5 to 7 MPa). It was found that 0.15 mm of axial shortening was enough to allow an accurate creep strain rate to be determined. This cycle was then repeated sequentially until the sample eventually failed, usually after about 10 to 14 days. Implementation of the stress-stepping methodology is illustrated in Figure 12, which shows the last two stress steps imposed during the final 3.5 hours of a ten day experiment.

[21] In order to verify this methodology, we compared results from conventional and stress-stepping creep tests conducted on samples of DDS under the same experimental conditions. The results are given in Figure 13, which shows the creep strain rates from a set of conventional experiments and a single stress-stepping experiment, all run at a Peff of 30 MPa. We note that the trends observed in the stress dependence of the creep train rates is virtually identical, but that the curves are somewhat offset. We attribute this offset to the problem of natural sample variability noted above. Having demonstrated that the stress-stepping technique can replicate the creep strain rate dependence on Q, we then used it to investigate the influence of Peff on brittle creep at a Peff of 10, 30 and 50 MPa (while maintaining a constant

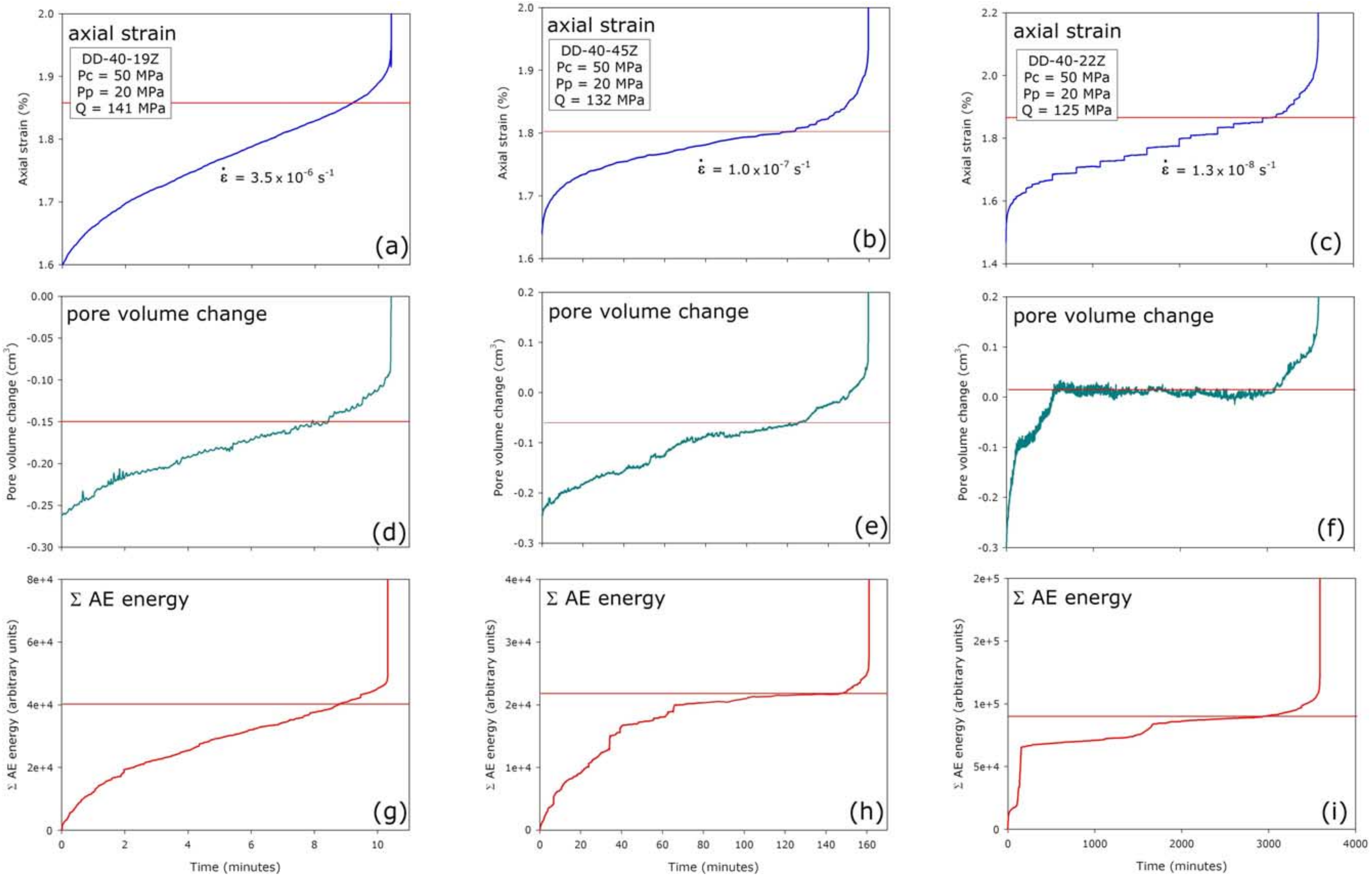

Figure 7. Graphs of the three damage proxies for three conventional brittle creep experiments on water-saturated DDS that have yielded creep strain rates over three orders of magnitude: 1.3×10^{-8}, 1.0×10^{-7}, and 3.6×10^{-6}. (a–c) Time-strain (creep) curves. (d–f) Pore volume change curves. (g–i) Output of AE energy for the three experiments. The position of the onset of accelerating tertiary creep is indicated in each figure by a horizontal line. Experimental conditions are also indicated on the figures. Pc, confining pressure; Pp, pore fluid pressure; Q, applied differential stress.

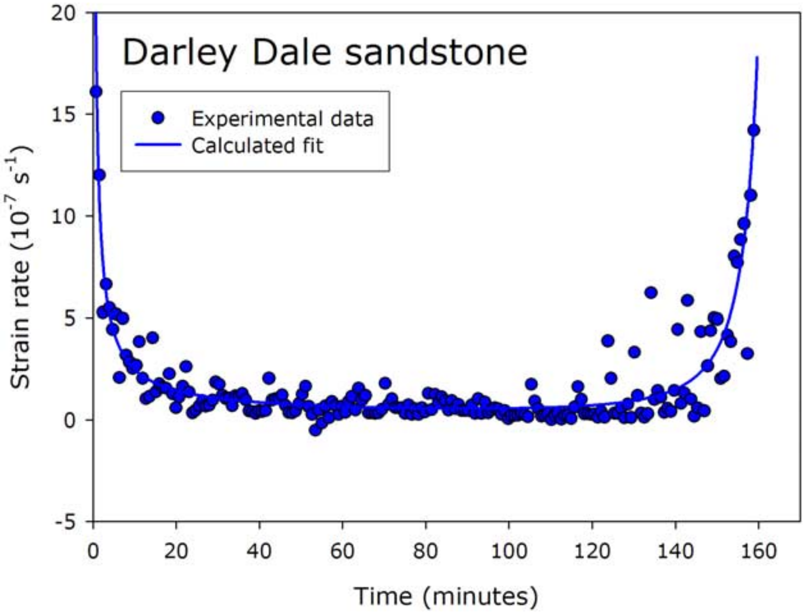

Figure 8. "Bathtub plot" of the first derivative of the experimental strain data from a conventional creep experiment on DDS that yielded a creep strain rate of 1.0×10^{-7} s^{-1} against time. Experimental conditions are indicated on Figure 7b. Data are from experiment DD-40-45Z.

Pp of 20 MPa). The results are given in Figure 14, which shows that varying the Peff, even over this modest range, has a profound influence on creep strain rates. Firstly, the strain rates are shifted to dramatically lower values for the same Q as Peff is increased. This appears consistent with the results from constant strain rate experiments showing that DDS is stronger at a higher Peff (Figure 6). However, the increase in strength seen in constant strain rate experiments as Peff is increased from 10 to 50 MPa is about 80%, while the decrease in creep strain rate over the same interval is many orders of magnitude. Secondly, the gradients of the curves on Figure 14 describing the relation between creep strain rate and Q decrease significantly as Peff is increased.

[22] Since it is possible that an increased presence of water molecules may influence the rate of stress corrosion reactions, we also used stress-stepping experiments to investigate the possible influence of Pp on brittle creep at constant Peff. Experiments were run at a fixed Peff of 30 MPa, but with a Pp of 20 and 40 MPa. The results are presented in Figure 15. The two creep curves are very close and there is no difference in their gradients; furthermore, the creep strain rates at a Pp of 40 MPa are lower than those at 20 MPa. The small offset between the two creep curves is however within the range expected from sample variability and we are therefore unable to state, from our limited data, whether doubling the Pp has any influence on the creep rate or not.

5. Discussion

5.1. The Observable Range of Brittle Creep Behavior

[23] The range of brittle creep behavior observed in this study is plotted in effective confining pressure-applied differential stress (Peff-Q) space in Figure 16. As noted in the introduction, in order to perform brittle creep experiments in a feasible laboratory timescale we restricted ourselves to the range of Q between D' and σ_p. It is likely that brittle creep can occur at any Q above C'; however, brittle creep close to C' is likely to be extremely slow and therefore impracticable to study over any reasonable laboratory timescale. Given that C' marks the lower limit of dilatant cracking (and the lower limit of new damage accumulation) we suggest that brittle creep is unlikely to occur below this limit.

5.2. Creep Stain Rates and Damage Levels

[24] Our conventional brittle creep experiments (all conducted at a constant Peff of 30 MPa) demonstrate that creep strain rate and time-to-failure in porous sandstone are strongly dependent on Q; an observation previously noted for creep in sandstones [*Baud and Meredith*, 1997; *Ngwenya et al.*, 2001]. A comparison between our data and those of *Baud and Meredith* [1997], under the same Peff conditions (30 MPa), is given in Figure 17 and also in Table 3. The gradients of the two curves on Figure 17 are remarkably similar and, again, the slight offset can be explained by sample variability.

[25] The results from our conventional creep experiments also demonstrate that the three measured proxies for crack damage (axial strain, pore volume change and output of AE energy) have approximately equal values at the transition from secondary to tertiary creep (marked by horizontal lines in Figure 7). This holds for all creep strain rates (measured during secondary creep) over the three orders of magnitude sampled. As noted earlier, this suggests that there is a critical level of damage required before the onset of acceleration to failure. This observation of a critical damage threshold for the onset of tertiary creep has previously been reported from a number of experimental studies [e.g., *Griggs*, 1939, 1940; *Wawersik and Brown*, 1973; *Cruden*, 1974; *Kranz and Scholz*, 1977; *Baud and Meredith*, 1997], and has also been predicted from modeling [*Armitrano and*

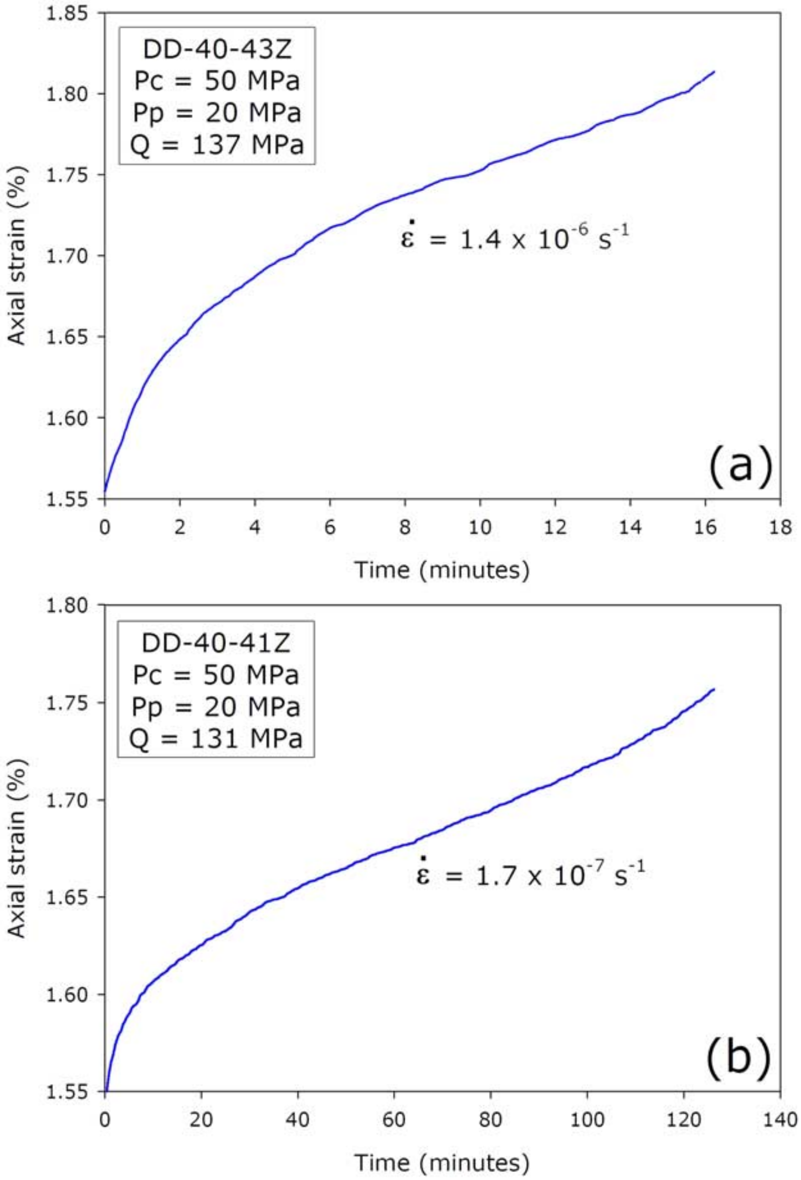

Figure 9. Axial strain against time for the two experiments designed to investigate the rock microstructure at the onset of accelerating tertiary creep at (a) 1.4×10^{-6} and (b) 1.7×10^{-7} s^{-1}. Experimental conditions are displayed on the figure. Pc, confining pressure; Pp, pore fluid pressure; Q, applied differential stress.

Table 2. Quantitative Microstructural Data From Optical Microscopy Analysis on an Undeformed Sample of DDS, Samples of DDS Taken to the Onset of the Tertiary Creep Phase Under Different Creep Strain Rates, and a Postfailure Sample of DDS[a]

Sample Conditions	Crack Density for Linear Intercepts Normal to σ_1 $P_\perp$ (mm^{-1})	Crack Density for Linear Intercepts Parallel to σ_1 $P_\parallel$ (mm^{-1})	Crack Area per Unit Volume P_v (mm^{-1})	Crack Anisotropy A_c
Undeformed	0.41	0.38	0.81	0.08
Onset of tertiary creep at 1.7×10^{-7} s^{-1}	0.59	0.45	1.11	0.27
Onset of tertiary creep at 1.4×10^{-6} s^{-1}	0.53	0.42	1.00	0.24
Postfailure	2.97	1.46	5.29	0.68

[a] See text for details on measurement technique.

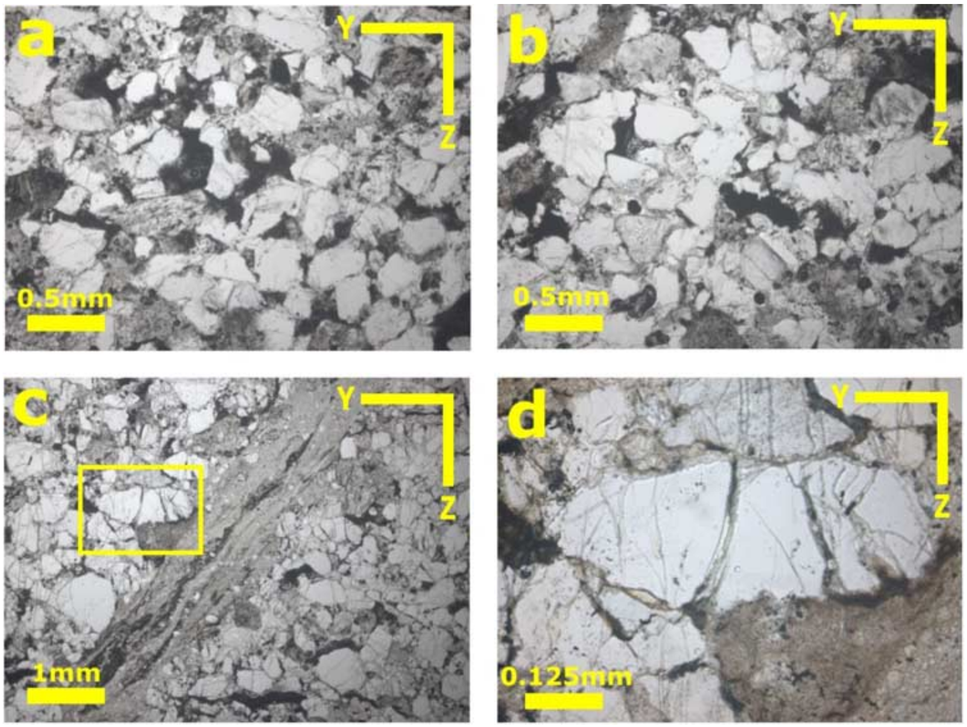

Figure 10. Photomicrographs of samples of DDS under plane-polarized light used for the investigation into the spatial distribution and density of microcracks. (a) Sample taken to the onset of accelerating tertiary creep at 10^{-6} s^{-1} (Figure 9a). (b) Sample taken to the onset of accelerating tertiary creep at 10^{-7} s^{-1} (see Figure 9b). (c) Shear band within sample taken to failure in a conventional brittle creep experiment. (d) Magnified image of the rectangle shown in Figure 10c showing the microcracks present within the grains near the shear band. *Z* axis is normal to the axial loading direction. Photomicrographs of an undeformed sample can be found in Figure 2.

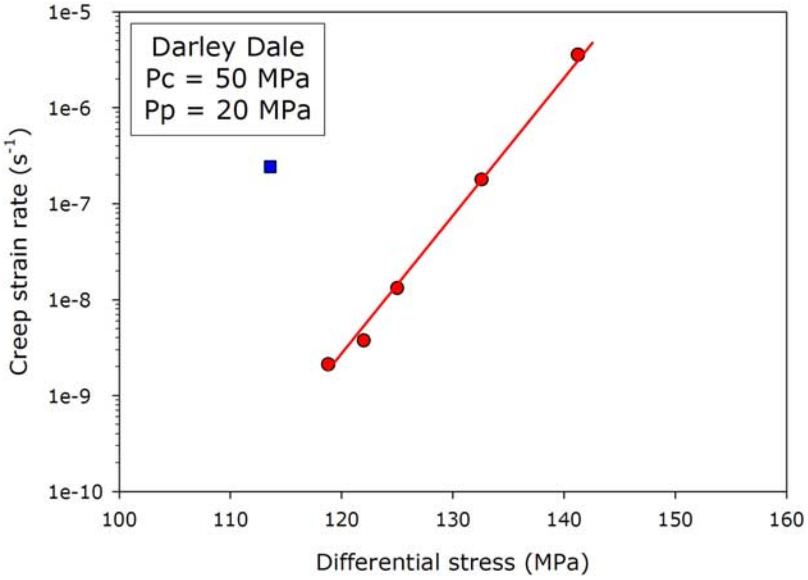

Figure 11. Creep strain rate data from multiple conventional brittle creep experiments on water-saturated DDS plotted on a semilog scale against applied differential stress (circles). Experimental conditions are displayed on the figure, and the error bars are represented by the size of the data points. The square represents a conventional brittle creep experiment that highlights the problem associated with sample variability during conventional brittle creep experiments (see text for details). Pc, confining pressure; Pp, pore fluid pressure.

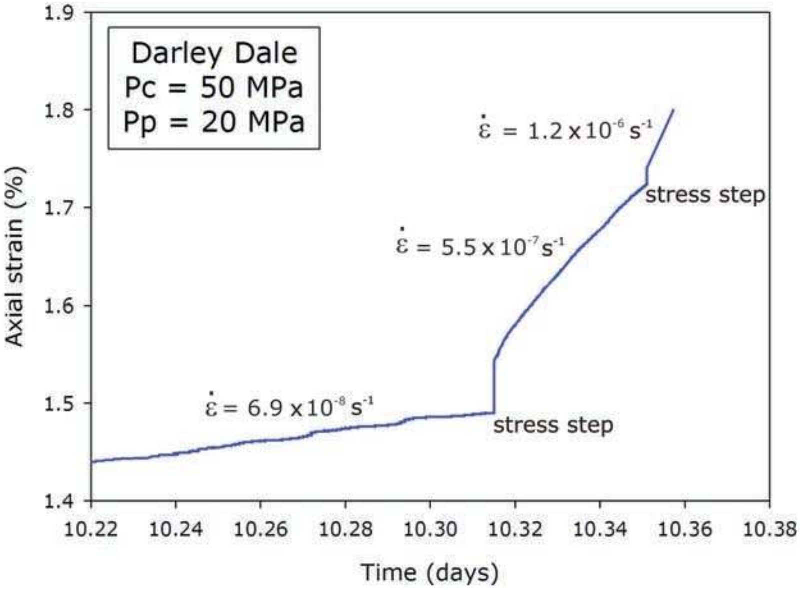

Figure 12. Graph of axial strain against time to demonstrate the methodology behind the stress-stepping brittle creep experiments. The figure shows the stress steps and from where the creep strain rates were calculated. The sample in this experiment failed after 10.36 days.

Helmstetter, 2006]. In particular, *Kranz and Scholz* [1977] reported that tertiary creep only commenced when the rock had sustained a critical amount of inelastic volumetric strain. *Baud and Meredith* [1997] support this observation and reported that a critical level of volumetric strain (as measured by pore volume change) was required to induce tertiary creep. Furthermore, they demonstrated that a critical level was required in their other proxy measures of damage (axial strain and output of AE energy) before the onset of tertiary creep. They suggested that this point also marked the onset of localization of damage, leading to acceleration to failure on a localized fault zone regardless of Q and the creep strain rate.

[26] In order to address this point further, we have investigated samples that were taken to the onset of tertiary creep and then unloaded and removed from the deformation

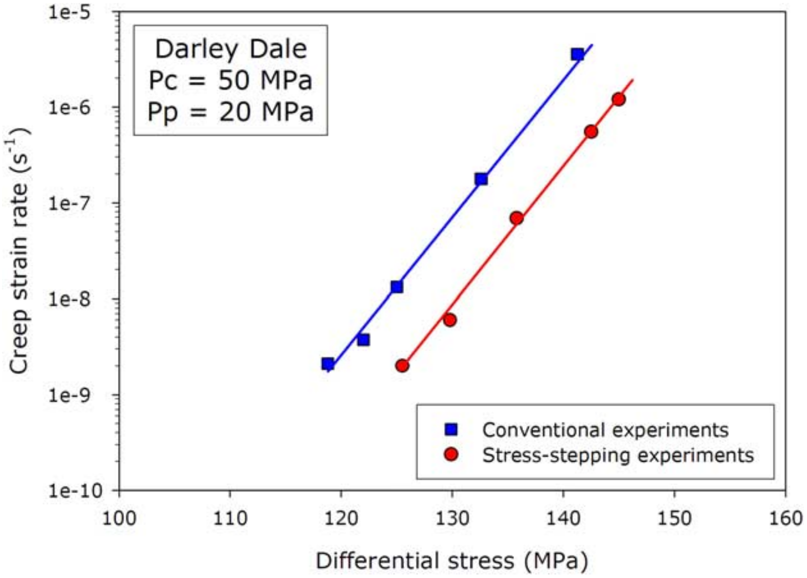

Figure 13. Creep strain rate data from a stress-stepping brittle creep experiment on water-saturated DDS (circles) plotted side-by-side with those data derived from conventional brittle creep experiments (squares). Creep strain rate data are plotted on a semilog scale against applied differential stress. The horizontal shift in the experimental curves is due to initial sample variability (see text for details). Experimental conditions are displayed on the figure, and the error bars are represented by the size of the data points. Pc, confining pressure; Pp, pore fluid pressure. Step-creep experiment data from samples DD-40-15Z (see Table 3).

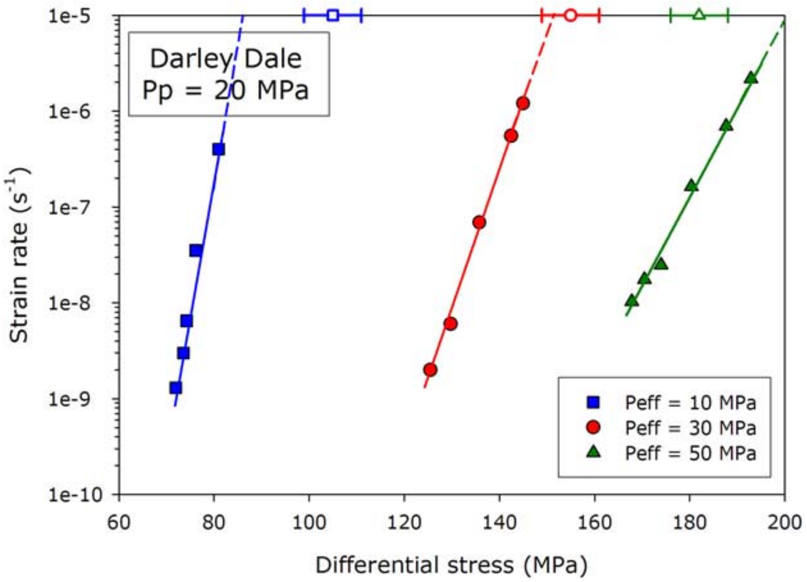

Figure 14. Creep strain rate data from stress-stepping brittle creep experiments performed at 10 (solid squares), 30 (solid circles), and 50 MPa (solid triangles) effective confining pressures on water-saturated DDS while maintaining a constant pore fluid pressure of 20 MPa. Short-term peak stress data from constant strain rate (1.0×10^{-5} s^{-1}) experiments are plotted as open shapes. All strain rate data are plotted on a semilog scale against applied differential stress. Error bars are represented by the size of the data points, and the range of short-term peak stresses observed in constant strain rate experiments is indicated by the horizontal bars. Stress-stepping creep experiments: 10 MPa effective confining pressure, sample DD-40-28Z; 30 MPa effective confining pressure, sample DD-40-15Z; 50 MPa effective confining pressure, sample DD-40-32Z (see Table 3). Pp, pore fluid pressure.

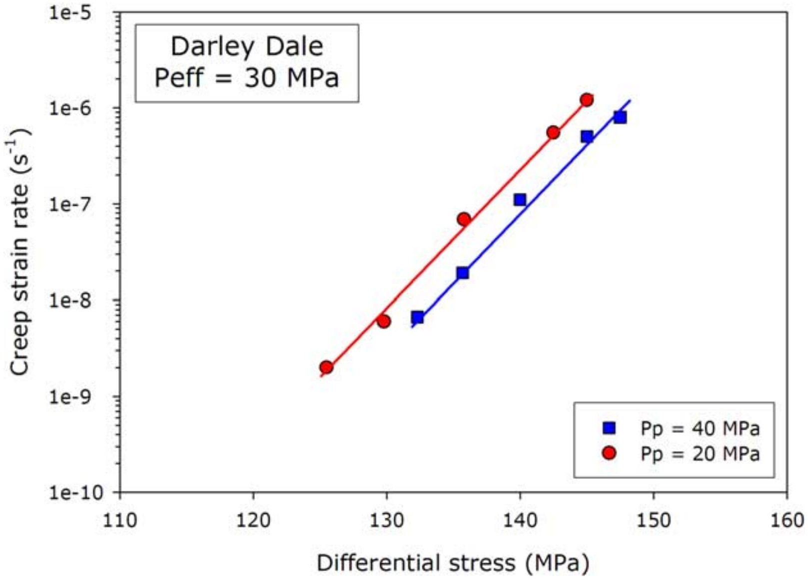

Figure 15. Creep strain rate data from stress-stepping brittle creep experiments on water-saturated DDS performed at 20 (circles) and 40 MPa (squares) pore fluid (distilled water) pressure while maintaining a constant 30 MPa effective confining pressure. Creep strain rate data are plotted on a semilog scale against applied differential stress. Experimental conditions are displayed on the figure, and the error bars are represented by the size of the data points. 20 MPa pore fluid pressure, sample DD-40-15Z; 40 MPa pore fluid pressure, sample DD-40-35Z (see Table 3). Pp, pore fluid pressure; Peff, effective confining pressure.

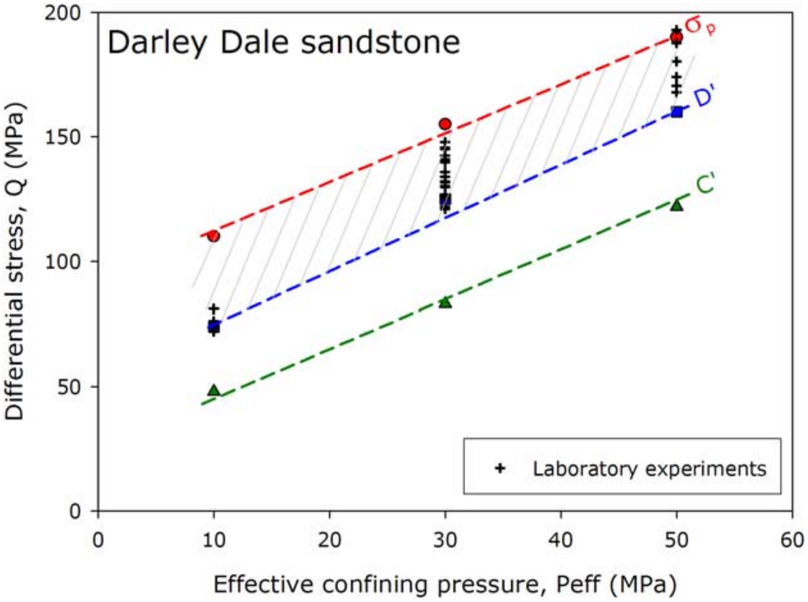

Figure 16. Effective confining pressure; differential stress (Peff-Q) diagram for the experimental creep data collected for DDS during this study. The laboratory creeping range is marked by the hatched area. The figure includes experimentally derived values for the short-term peak stress (circles), D' (squares), and C' (triangles) at effective confining pressures of 10, 20, and 30 MPa from constant strain rate (1.0×10^{-5} s^{-1}) experiments. Experimental creep data from both conventional and stress-stepping experiments are included on the figure (cross hairs).

apparatus for microstructural analysis. For all samples, linear crack densities ($P_{\perp}$ and $P_{\|}$) were determined by the technique described earlier, and the results are given in Table 3 together with measurements of crack area per unit volume (P_v) and crack anisotropy (A_c). P_v increases by between 24 and 37% in both samples taken to the onset of tertiary creep from the values for the initial, undeformed state. While these increases are significant, more important is the increase in crack anisotropy. In the undeformed state the anisotropy is very low at 8%, while at the onset of tertiary there is a threefold increase to between 24 and 27%. This is strong evidence that the new damage induced during

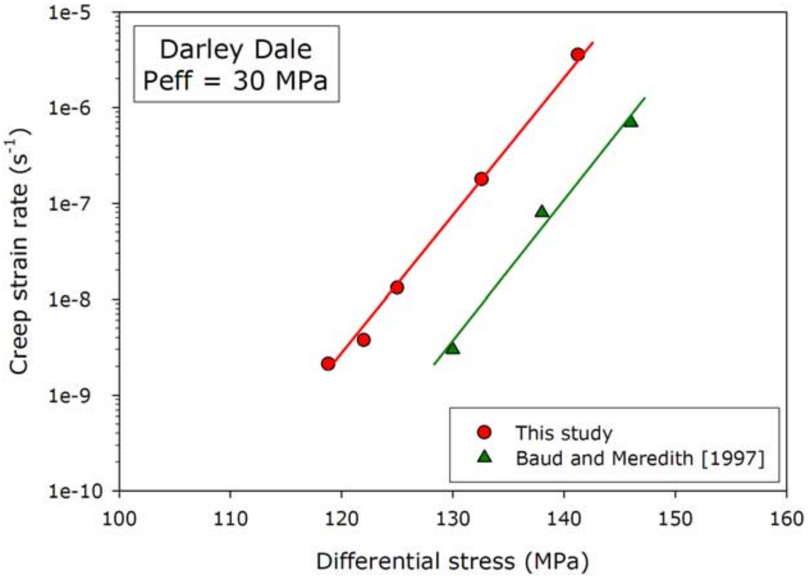

Figure 17. Creep strain rate data from stress-stepping brittle creep experiments on water-saturated DDS at 30 MPa effective confining pressure from this study (circles) and from conventional brittle creep experiments on water-saturated DDS at 30 MPa effective confining pressure from *Baud and Meredith* [1997] (triangles). Creep strain rate data are plotted on a semilog scale against applied differential stress. Experimental conditions are displayed on the figure, and the error bars are represented by the size of the data points. Stress-stepping experiment, sample DD-40-15Z. Peff, effective confining pressure.

Table 3. Experimental Conditions and Results of Regression Analysis for Power Law and Exponential Function Fits to the Creep Strain Rate Data for All the Creep Experiments in This Study (See Text and Equations (1) and (2) for Details)

Sample Number	Confining Pressure (MPa)	Pore Pressure (MPa)	Effective Confining Pressure (MPa)	Power Law Gradient Function (η)	Exponential Law Gradient Function (β)	Power Law Fit R^2 Value	Exponential Law Fit R^2 Value
DD-40-15Z	50	20	30	45.40	0.335	0.996	0.996
DD-40-44Z	50	20	30	44.06	0.323	0.997	0.998
DD-40-28Z	30	20	10	49.93	0.650	0.984	0.981
DD-40-32Z	70	20	50	39.29	0.218	0.991	0.992
DD-40-35Z	70	40	30	45.47	0.325	0.994	0.992
Conventional creep experiments	50	20	30	44.10	0.340	0.994	0.996
Baud and Meredith [1997]	75	45	30	47.05	0.341	0.990	0.986

primary and secondary creep is dominated by the growth of axial cracks subparallel to the maximum principal stress [*Lawn*, 1993]. The crack densities and anisotropy for both samples have similar values in spite of the order of magnitude difference in creep strain rate. However, for the sample taken to failure, all the measures of crack density and the anisotropy increase substantially, as expected. Crack density values from both undeformed and postfailure samples in this study compare well with those previously published for DDS [*Wu et al.*, 2000]. The level of crack damage at the onset of tertiary creep is very similar to that for a sample taken to the prepeak stress stage in a constant strain rate experiment presented by *Wu et al.* [2000]. This should not be surprising, since both conditions represent a point that is well into the phase of dilatant cracking but that precedes crack coalescence and damage localization.

[27] To further investigate the time evolution and spatial distribution of cracking during brittle creep, we determined the locations of AE hypocenters during conventional brittle creep experiments on DDS at a Peff of 30 MPa (Pc of 50 MPa and a Pp of 20 MPa). Numerous previous studies have shown that AE output increases exponentially or supraexponentially as stressed rock approaches macroscopic failure [e.g., *Scholz*, 1968b; *Sammonds et al.*, 1992; *Cox and Meredith*, 1993; *Fortin et al.*, 2006; *Stanchits et al.*, 2006], and multichannel recording systems have been used to determine the location of AE hypocenters of the AE output within the sample [*Lockner et al.*, 1991, 1992; *Lockner and Byerlee*, 1992; *Lockner*, 1993b; *Zang et al.*, 1996; *Lei et al.*, 2000; *Lei et al.*, 2004]. More recently, Giga-RAM recorders have been used to capture continuous AE waveforms during rock deformation experiments to allow even more sophisticated analysis [*Thompson et al.*, 2006; *Benson et al.*, 2007; *Townend et al.*, 2008].

[28] For our experiments, we selected values of Q that produced a creep strain rate of approximately 10^{-7} s^{-1} so that the secondary creep phase was long enough (about 150 minutes) to allow us to determine the locations of a sufficient number of AE hypocenters to follow the evolution of crack damage with time. Figure 18 shows the located AE events from one such experiment in which the strain rate during secondary creep was 1.4×10^{-7} s^{-1}. A total of 1877 AE hypocenters were located during the experiment, of which 592 occurred during the primary creep phase, 702 during secondary creep and 583 during tertiary creep. During primary creep (Figure 18a) the AE hypocenters form two diffuse clusters in the upper and lower parts of the sample that cover the full sample diameter. During secondary creep the hypocenter locations become more evenly distributed through the sample volume (Figure 18b). During tertiary creep (Figure 18c) the pattern becomes a little more complicated. We observe both a distributed pattern of hypocenters and, superimposed on this, a set of localized hypocenters that locate along the eventual fault plane. The AE events that produce these localized hypocenters occurred during that latter part of tertiary creep as the fault propagated rapidly across the sample to produce dynamic, macroscopic failure. With the benefit of hindsight, it could be argued that there is some indication of localization in the locations determined during secondary creep, but this is only apparent after looking at the tertiary creep data. The total number of located AE hypocenters during all three phases is shown in Figure 18d, with the orientation of the eventual shear failure plane superimposed. The pattern seen in Figure 18 is characteristic of all our experiments in which AE hypocenter locations were investigated. In general, AE behavior is (1) diffuse and distributed during primary creep, (2) distributed with some suggestion of localization or “mixed mode” during secondary creep and (3) increasingly localized during tertiary creep.

[29] The suggestion that AE clustering might commence during the latter part of secondary creep appears to conflict with the idea of a critical damage threshold for the onset of tertiary creep and localization of deformation [e.g., *Baud and Meredith*, 1997]. However, we suggest that this merely highlights the difficulty of defining the onset of tertiary creep from an emergent strain-time curve. It may well be that the transition would actually be better defined using all the available AE data (hit rate, energy rate and hypocenter locations). While there have been a number of studies that have monitored AE output during brittle creep experiments on rock [e.g., *Wu and Thomsen*, 1975; *Lockner and Byerlee*, 1975; *Ohnaka*, 1983; *Yanagidani et al.*, 1985; *Nishizawa et al.*, 1984; *Hirata et al.*, 1987; *Nishizawa and Noro*, 1990; *Baud and Meredith*, 1997], only a few have used the location of AE hypocenters to investigate the transition from distributed to localized deformation as samples approach failure. Furthermore, with the exception of *Hirata et al.* [1987], these have all been conducted on dry crystalline rock samples under uniaxial compression [*Yanagidani et al.*, 1985; *Nishizawa et al.*, 1984; *Hirata et al.*, 1987; *Nishizawa and Noro*, 1990]. Under such uniaxial conditions, localization of AE event hypocenters is reported to have commenced during secondary, or even primary [*Yanagidani et*

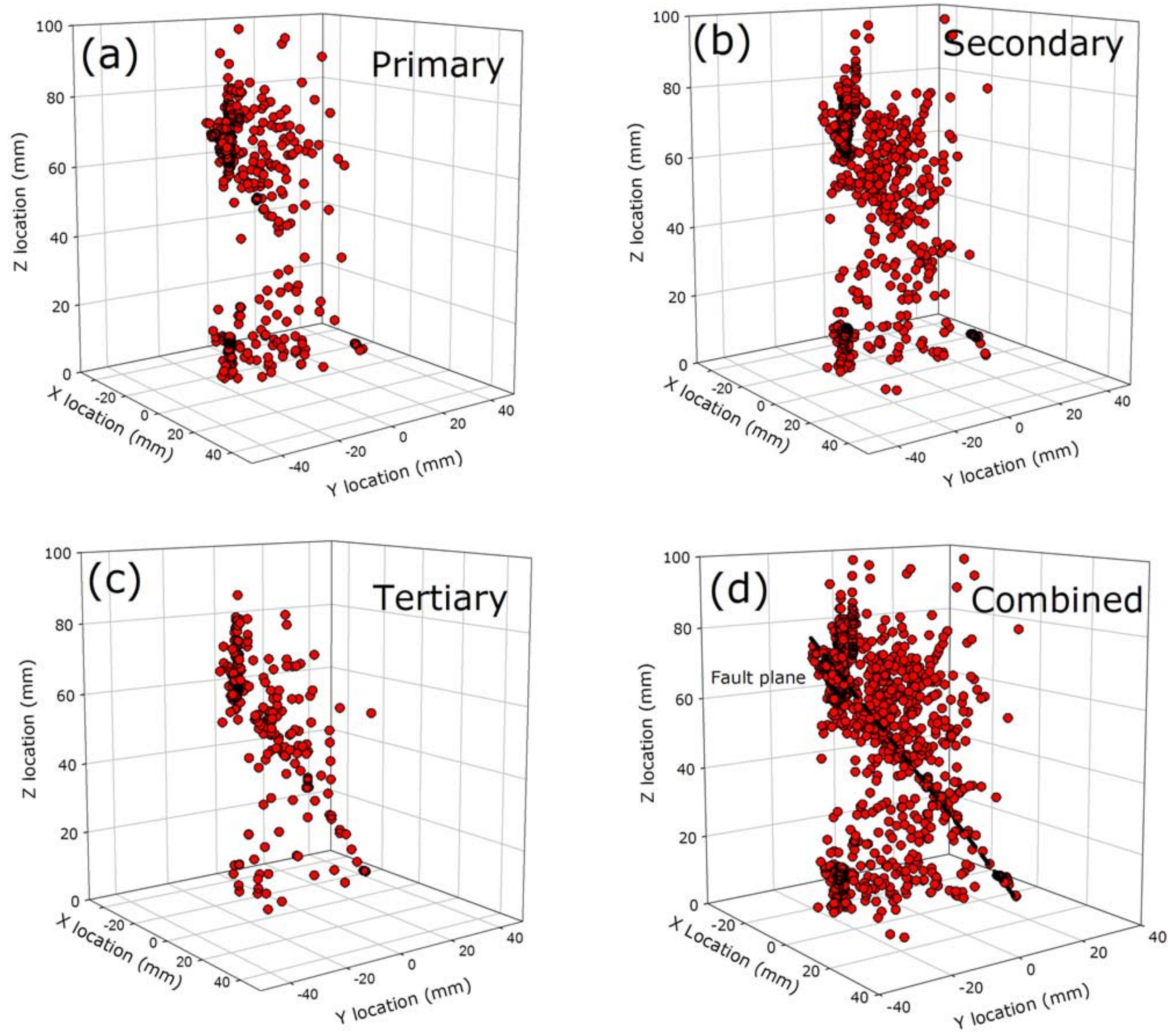

Figure 18. Plots of the calculated AE hypocenters for (a) primary creep, (b) secondary creep, (c) tertiary creep, and (d) the total of all three of the creep phases for a conventional brittle creep experiment at a creep strain rate of 1.4×10^{-7} s^{-1}. The combined plot in Figure 18d also shows the location of the eventual fault plane. *Z* axis is normal to the axial loading direction.

al., 1985], creep. This is as expected, since axial crack extension is not suppressed by the application of a Pc, and samples can fail by axial splitting rather than shear faulting associated with failure under triaxial compression [*Paterson and Wong*, 2005]. By contrast, *Hirata et al.* [1987] located AE hypocenters during brittle creep of dry granite under triaxial stress conditions. They calculated an evolving spatial fractal dimension of AE events by cross correlation of hypocenter locations, and reported that their fractal dimension decreased as creep progressed. This indicates that clustering and localization increases as creep progresses, with the biggest changes occurring during the tertiary creep phase.

5.3. The Influence of Confining Pressure and Pore Fluid Pressure on Creep Strain Rates

[30] Results from our stress-stepping creep experiments have demonstrated that creep strain rates are dramatically reduced for the same level of Q when the Peff is increased (Figure 14). This is at least partially expected, since it well known that rock strength increases with increasing Peff [e.g., *Paterson*, 1958; *Byerlee*, 1967; *Francois and Wilshaw*, 1968; *Rummel and Fairhurst*, 1970; *Wawersik and Brace*, 1971; *Ohnaka*, 1973; *Baud et al.*, 2000]. For example, in our constant strain rate experiments (Figure 6) we see an increase in strength of about 70% (from 105 MPa to 180 MPa) as Peff is increased from 10 to 50 MPa, these data are also plotted as open symbols on Figure 14 and show that a substantial decrease in creep strain rate can be expected from the purely mechanical effect of increasing Peff. However, this mechanical influence of the Peff is not sufficient to explain all of the observed decreases we observe in the creep strain rate over the same pressure interval (Figure 14). We therefore suggest that the remainder of the observed shift is due to the chemical influence of

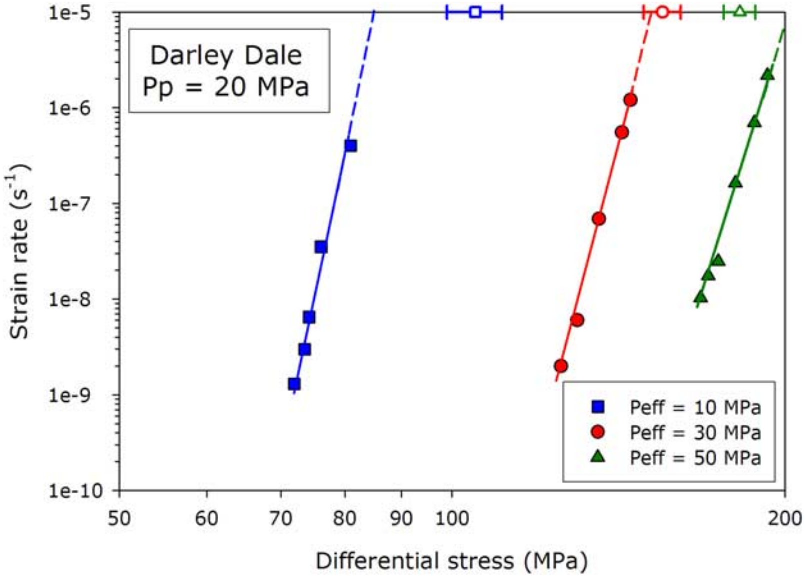

Figure 19. Creep strain rate data from stress-stepping brittle creep experiments performed at 10 (solid squares), 30 (solid circles), and 50 MPa (solid triangles) effective confining pressures on water-saturated DDS while maintaining a constant pore fluid pressure of 20 MPa. Short-term peak stress data from constant strain rate (1.0×10^{-5} s^{-1}) experiments are plotted as unfilled shapes. All strain rate data are plotted on a log-log scale against applied differential stress. Experimental conditions are displayed on the figure, and the error bars are represented by the size of the data points. 10 MPa effective confining pressure, sample DD-40-28Z; 30 MPa effective confining pressure, sample DD-40-15Z; 50 MPa effective confining pressure, sample DD-40-32Z (see Table 3).

water. Furthermore, the shifts in the strain rate curves appear to decrease with increasing Peff, and we suggest that the chemically driven process of stress corrosion cracking that drives brittle creep is therefore inhibited at a higher Peff in our DDS samples. This is entirely consistent with the suggestion that stress corrosion is inhibited at higher Peff due to a decrease in water mobility (i.e. the diffusion of the reactive species to the bonds at crack tips) because of a reduction in crack aperture [*Atkinson and Meredith*, 1987].

[31] These observations are consistent with the results of the systematic study on the influence of Peff on brittle creep in granite [*Kranz*, 1980], which showed that increasing the Peff led to an increase in the overall time-to-failure (equivalent to a decrease in the strain rate). *Kranz* [1980] also postulated that the increase in Peff led to a decrease in the rate at which corrosive chemical species could reach crack tips, and also to a decrease in the rate of crack interaction prior to the onset of tertiary creep. However, the study is limited by the fact that it was performed on air-dry samples in the absence of pressurized pore fluid.

[32] Subsequent work has highlighted the importance of using wet samples [*Kranz et al.*, 1982; *Meredith and Atkinson*, 1983]. Other studies on the influence of Peff on brittle creep can be found in *Wawersik and Brown* [1973] and *Ngwenya et al.* [2001]. *Wawersik and Brown* [1973] performed creep experiments on sandstone and granite at a Peff of 7, 35 and 70 MPa and found that an increase in Peff resulted in a decrease in creep strain rates. *Ngwenya et al.* [2001] also performed stress-stepping brittle creep experiments, where multiple measurements are made on the same rock sample. They found that the influence of increasing Peff is to shift the individual curves of strain rate systematically toward a higher Q; in accordance with the law of effective stress. For Gyda sandstone, an increase in Peff from 17.2 MPa to 34.5 MPa shifted creep strain rate curves by about 45 MPa along the *x* axis. This is approximately the same shift observed in our experiments (55 MPa shift for an increase in Peff of 20 MPa).

[33] In the data of Figure 14, we note that not only are the curves shifted to lower strain rates as Peff is increased, but that they also appear to decrease in gradient. A gradient in the strain rate − Q curves is entirely as expected since it is known that rock strength increases with an increase in strain rate [*Paterson and Wong*, 2005]. However, it is not clear if this can explain the observed change in gradient, or if it is due to a combined mechanical and chemical effect. We are unable to discriminate between these two effects on the basis of the current data. This would require further measurements on both saturated and dry samples over a range of constant and creep strain rates. This change in gradient is emphasized by the log linear nature of the plots in Figure 14 (i.e., an exponential fit). However, it has previously been noted by *Main* [2000] that it is difficult to discriminate between exponential and power law fits to brittle creep data given the relatively narrow range of experimental data currently available. For comparison, we have therefore provided a log-log plot of the same data in Figure 19. We discuss the comparison of exponential and power law fits to creep data in detail in section 5.3 below.

[34] The chemical activity of water is enhanced by elevated pressure [*Fyfe et al.*, 1978]. Therefore if chemically enhanced stress corrosion cracking is the mechanism responsible for inducing brittle creep, we might expect creep rates to be enhanced at a higher Pp even when the

Peff was held constant. We have investigated this in stress-stepping experiments and the data are shown in Figure 15. However, as previously noted, our results suggest that doubling the Pp from 20 to 40 MPa, while maintaining the Peff constant at 30 MPa, influenced creep strain rates within the range expected from natural sample variability. We are therefore unable, from our limited data set, to unequivocally rule out any potential Pp influence on creep strain rates. However, if the results can be explained by sample variability then this implies that the rate at which reactive species can diffuse through the sample to crack tips is the limiting control on stress corrosion reactions, rather than the amount of reactive species present. However, we should also note that the chemistry of the pore fluid (initially, deionized distilled water) is likely to have changed during the 10 to14 days that the experiments lasted; a potentially important issue highlighted by *Ojala et al.* [2003].

5.4. Macroscopic Creep Laws

[35] In order to apply the concept of stress corrosion controlled, time-dependent cracking to large-scale geophysical problems, macroscopic creep models have been developed to describe this behavior, and are generally in one of two forms:
(1) power law form,

$$\dot{\varepsilon} = A(\sigma_d)^{\eta} \tag{1}$$

or (2) exponential form,

$$\dot{\varepsilon} = Ce^{\beta\sigma d} \tag{2}$$

Where ε is the creep strain rate, Q is the differential stress and A, C, β and η are all constants. The most widely used and accepted theory of stress corrosion is Charles' power law [*Charles*, 1958] and has been used to describe virtually all experimentally determined data for geological materials [see *Meredith and Atkinson*, 1983; *Atkinson*, 1984; *Swanson*, 1984]. However, exponential forms, such as the Charles-Hillig-Wiederhorn theory [*Charles and Hillig*, 1962; *Hillig and Charles*, 1965; *Wiederhorn and Bolz*, 1970], have so far been shown to describe creep behavior equally as well over the range of data achievable in the laboratory [see *Costin*, 1987; *Lawn*, 1993; *Lockner*, 1993a; *Ngwenya et al.*, 2001]. More recently, mean-field theory of damage mechanics have been developed [*Lockner*, 1998; *Main*, 2000] that invokes a two stage process: (1) a phase of strain hardening involving distributed crack damage, and (2) a phase of strain softening involving crack interaction and coalescence. Phase (1) dominates in the early stage of deformation and phase (2) dominates in the later stage of deformation. Such models also therefore postulate a critical damage threshold where crack interaction leads to a rapid acceleration to failure on a localized fault plane. As the stress intensity at a crack tip is influenced by the length of the crack, given suitable conditions, the nonlinear relation between strain rate and stress given by stress corrosion theory means the rate at which a crack grows in time can accelerate even under a constant boundary stress. For a population of cracks growing in a rock sample held at constant stress, this process is embodied by accelerating strain rate and AE emission with time. In field data, where it is difficult to determine the absolute stress conditions, accelerating strain and seismic activity have been used to infer an underlying stress corrosion mechanism. The rate of deformation precursors to volcanic eruptions show both power law and exponential accelerations with time [*Voight*, 1988, 1989], shown to be theoretically consistent with a stress corrosion process at constant boundary stresses [*Main*, 2000].

[36] The mean field model for damage evolution developed by *Main* [2000] is based on laboratory observations of subcritical crack growth in a variety of composite materials, where the crack velocity V scales with the n'th power of the stress intensity factor $K \sim V^n$. In some single crystal experiments, a plateau of constant velocity is seen at intermediate K due to diffusion-limited crack growth, but this is neglected in the model at this stage. Depending on the loading configuration and a stress feedback exponent q, K scales with stress σ and crack length c according to $K \sim \sigma c^q$ [*Costin*, 1987]. For $nq < 1$ these two equations predict decelerating crack growth (net negative feedback), and for $nq > 1$ accelerating crack growth toward a singularity at the failure time (net positive feedback). Local negative feedback will lead to more distributed deformation in the form of a distributed array of microcracks, whereas positive feedback to localized deformation on a dominant macrocrack or fault (illustrated in *Main et al.* [1993, Figure 1]). In the mean field theory (based on assuming similar behavior for the mean crack length $\langle c \rangle$, no explicit account is taken for crack-crack interactions, except implicitly on their net effect on the feedback parameter q.

[37] Assuming the degree of damage quantified by $\langle c \rangle$ is related to the strain, and a linear superposition of positive and negative feedback processes, the evolution of total strain, Ω with time is then:

$$\Omega(t) = \Omega_I(1 + t/T)^m + \Omega_{III}\left(1 + t/t_f\right)^{\tilde{v}} \tag{3}$$

The amplitudes Ω_I and Ω_{III} represent primary and tertiary creep components respectively, T is a transient time, t_f is the asymptotic failure time and m and v are positive power law exponents related to n and q. In the general case this amounts to 6 free parameters. However, this is the minimum for a hybrid model, because both processes involve three parameters: an amplitude (defining the stress axis scale) a time constant (defining the time axis scale) and a curvature term (here the power law exponent). When plotted on a graph equation (3) predicts the spontaneous emergence of a long phase of steady state creep at intermediate times between T and t_f i.e. there is no need to invoke a third process for such secondary creep. Equation (3) also predicts that the emergent "steady state" strain rate scales as a power law function of the creep stress [*Main*, 2000]. The AE hypocenter location plots in Figure 17 confirm that distributed deformation dominates in the primary creep phase, whereas more localized deformation dominates in the tertiary creep phase. The mixed nature AE hypocenter locations in the steady state phase validates the assumption in *Main* [2000] that secondary creep separate process, but an emergent phenomenon of primary and tertiary creep.

[38] Here we show that this mean-field damage mechanics power law model can closely reproduce the relation

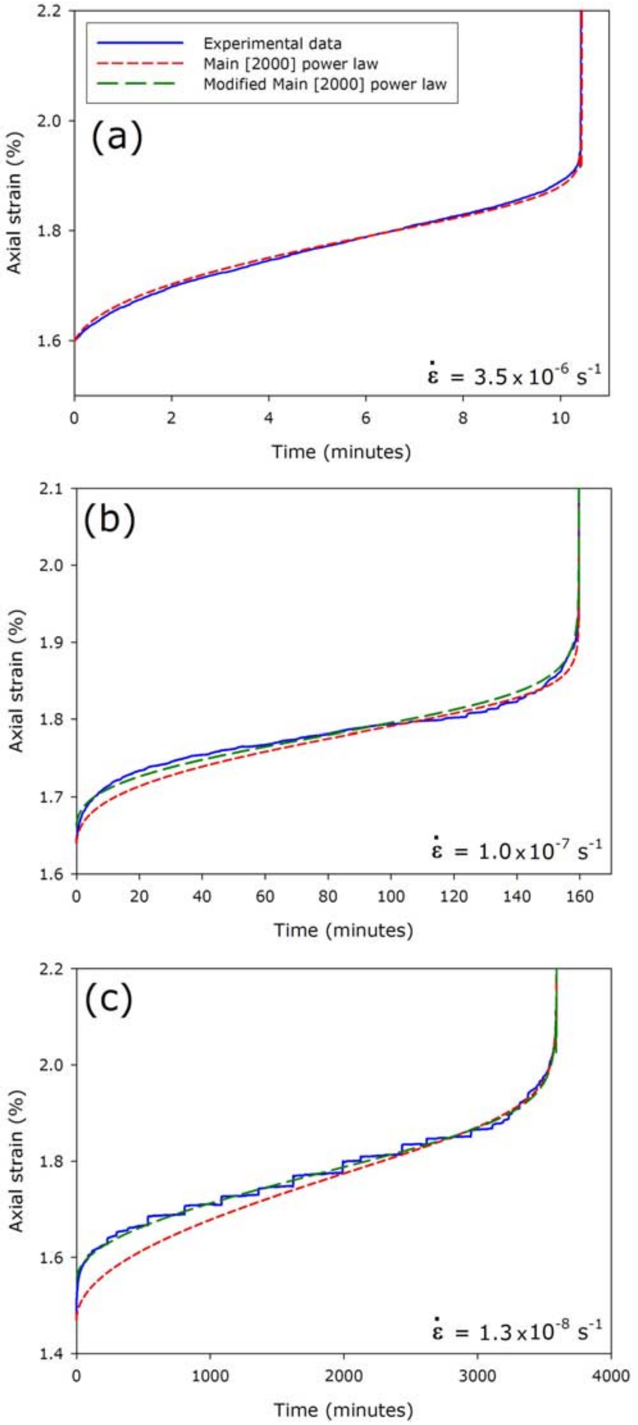

Figure 20. Axial strain against time for the three conventional brittle creep experiments shown in Figure 7 with the *Main* [2000] power law (short dashed lines) and modified *Main* [2000] power law (long dashed lines; see text for details) fits superimposed.

between strain and time observed in the conventional brittle creep experiments (Figure 20) i.e. that it is not necessary to invoke a separate process for secondary creep. Due to complexities of inversion associated with the nonlinearity in equation (3) we use a simple trial-and-error fitting technique and in the first instance assume a codependence between the two amplitude terms. The model is able to produce the closest fit to the data for faster creep strain rates and during the accelerating tertiary creep phase. At the slowest creep strain rates, the model does not accurately reproduce the initial primary creep phase. The likely cause of this discrepancy is the fact that equation (3) is based on mean-field damage mechanics that considers only the formation and interplay of cracks. At the lower stresses required to yield slow creep strain rates, processes such as pore space compaction could still be operative, explaining why the goodness of fit decreases with decreasing creep strain rate and why the model fits for tertiary creep despite the stain rate, since there will be only be the formation and coalescence of cracks at this point. To incorporate the potential additional pore closure mechanism, we refit the data with equation (3) but allowing Ω_I and Ω_{III} to vary independently. This is more consistent with the experimental data (Figure 20) and suggests that the relative amplitudes of the primary and secondary components can differ significantly. The parameters used in the models are displayed in Table 4.

[39] The parameters in Table 4 show that the amplitude of the decelerating process Ω_I is much smaller than that of the accelerating one Ω_{III}, by a few orders of magnitude, indicating that accelerating creep is the dominant process in terms of amplitude overall. Ω_{III} is relatively constant, whereas Ω_I decreases systematically as strain rate decreases, so that the relative importance of decelerating creep declines as the strain rate decreases. The failure time t_f increases systematically and nonlinearly over several orders of magnitude with decreasing strain rate, but the transient time T for transient creep is more stable, decreasing by a factor of 4 or so only at the very slowest strain rates. This may be because different reactions can be activated at slower strain rates, or that different minerals have different relative effects at lower strain rates. The power law exponent m for transient creep is remarkably consistent, with an exponent between 0.32 and 0.46 and no systematic change with strain rate. The power law exponent ν for accelerating creep is much smaller than m, indicating a much tighter curvature that can be seen on the normalized plots on Figure 20. The exponent ν ranges from 0.012 to 0.025, with more rapid acceleration at high strain rates. In future work automated nonlinear inversion procedures on all of the data sets will be used to ascertain if these small variations are significant, or whether a single solution for one or more of the optimal parameters can be found.

[40] Equation (3) is only one example of a macroscopic creep law. Exponential or logarithmic macroscopic creep law models have also been shown to fit experimental data

Table 4. Parameters Used in Equation (3) for the *Main* [2000] and Modified *Main* [2000] (See Text for Details) Models to Fit With the Experimentally Produced Creep Curves[a]

Creep Strain Rate (s^{-1})	Ω_I	Ω_{II}	τ_1	τ_3	m	v
3.6×10^{-6}	0.0400	1.5587	0.23	870.8	0.400	0.012
1.0×10^{-7}	0.0120	1.6275	0.22	15975.3	0.350	0.010
1.0×10^{-7} (mod)	0.0120	1.6500	0.22	11410.9	0.320	0.014
1.3×10^{-8}	0.0012	1.4679	0.05	143669.3	0.480	0.025
1.3×10^{-8} (mod)	0.0011	1.5500	0.05	143669.3	0.460	0.025

[a] The graphical representation of the macroscopic creep law fitting is shown in Figure 20.

over the laboratory range of creep strain rates [e.g., *Costin*, 1987; *Lawn*, 1993]. However, previous studies have shown that, over the creep strain rates achievable in the laboratory, it is not yet possible to distinguish between these functional forms [*Lockner*, 1993a; *Ngwenya et al.*, 2001; *Armitrano and Helmstetter*, 2006]. Further work, both experimental and statistical, is needed to rigorously distinguish between them, most critically to achieve a much broader bandwidth of strain rate.

6. Conclusions and Perspective

[41] Conventional creep experiments have shown that Q exerts a crucial influence on both creep strain rate and time-to-failure. They have also demonstrated that a critical level of damage needs to be reached before the onset of accelerating tertiary creep. Detailed microstructural analysis has shown that crack densities at the onset of tertiary creep are relatively low (compared with that of a sample taken to failure); however, conditions are likely to represent a point that is well into the phase of dilatant cracking but that precedes crack coalescence and damage localization. A threefold increase in crack anisotropy is seen between the undeformed state and the onset of tertiary creep. This is strong evidence that the new damage induced during primary and secondary creep is dominated by the growth of axial cracks subparallel to the maximum principal stress. Furthermore, crack densities and anisotropy are similar for samples taken to this point under creep strain rates that differ by an order of magnitude, supporting the idea of a critical damage threshold. AE hypocenter location analysis suggests that AE behavior during creep is (1) diffuse and distributed during primary creep, (2) distributed with some suggestion of localization or "mixed mode" during secondary creep and (3) increasingly localized during tertiary creep. The suggestion that AE clustering might commence during the latter part of secondary creep appears to conflict with the idea of a critical damage threshold for the onset of tertiary creep and localization of deformation [e.g., *Baud and Meredith*, 1997]. However, we suggest that this merely highlights the difficulty of defining the onset of tertiary creep from an emergent strain-time curve.

[42] Our experimental data has demonstrated the fundamental characteristics of brittle creep in sandstone, such as sensitivity to Q, as well as the contribution of variables such as Peff and Pp. Data derived from our stress-stepping experiments have been shown to compare favorably with those from conventional creep experiments. Stress-stepping creep experiments have shown that an increase in Peff inhibits the process of stress corrosion. We suggest that the most likely cause is a decrease in water mobility due to a reduction in crack aperture at a higher Peff. The opposite is true for a reduction in Peff. However, a two-fold increase in Pp, while maintaining a constant Peff, is shown to influence the rate of stress corrosion within the range expected from natural sample variability. However, if the results can be explained by sample variability then this implies that the rate at which reactive species can diffuse through the sample to crack tips is the limiting control on stress corrosion reactions, rather than the amount of reactive species present.

[43] We also show that mean-field damage mechanics power law modeling can closely reproduce the relation between strain and time observed in our conventional brittle creep experiments and that it is therefore not necessary to invoke a separate process for secondary creep. However, at the slowest creep strain rates, the *Main* [2000] model does not accurately reproduce the initial primary creep phase. The likely cause of this discrepancy is the fact that it is based on mean-field damage mechanics that considers only the formation and interplay of cracks. During the primary creep phase, additional pore space compaction processes could be still be operative. Allowing the variables to act independently, creating a modified *Main* [2000] model, incorporates the potential additional mechanism and is more consistent with the experimental data during the primary creep phase.

[44] We have presented data under the physical conditions appropriate to approximately 1.5–2 km depth in the Earth. At such depths, and assuming an average geothermal gradient of 30°C/km, the temperature of crustal rock would be between 45–75°C. Temperature has been previously noted to affect subcritical crack growth of a single crack in double-torsion experiments on synthetic quartz and dolerite [*Atkinson*, 1979; *Meredith and Atkinson*, 1982, 1983, 1985] and dramatically decrease time-to-failure under a constant load in conventional creep experiments on granite [*Kranz et al.*, 1982]. Also, the effect of a corrosive reactive species [*Atkinson and Meredith*, 1981] has been previously shown to influence single crack growth rate in double-torsion experiments on rock. However, it is unclear as to the effect of elevated temperature and corrosive reactive species on brittle creep strain rates where cracks can interact and coalesce under a Pc. Future studies should therefore concentrate on the effect of temperature and corrosive fluids on the creep strain rate in rock.

[45] **Acknowledgments.** We thank Neil Hughes, Steve Boon, and John Bowles for help and support during experimentation and Rosie Smith, Almar de Ronde, and Simon Hunt for their help. Thin sections were skillfully prepared by D. Mann (High Mesa Petrographics, Los Alamos, New Mexico, USA) and Jim Davy assisted with the SEM work. M. Heap was funded by NERC studentship NER/S/A2005/13553 and A. Bell by the EU "NERIES" project. This work was also partly funded by a Royal Society/CNRS International Joint Project award. We also thank Yves Guéguen, Dan Faulkner, Ernie Rutter, Teng-fong Wong, and one anonymous reviewer for comments that helped improve the manuscript.

References

Anderson, O. L., and P. C. Grew (1977), Stress corrosion theory of crack propagation with applications to geophysics, *Rev. Geophys.*, *15*, 77–104.

Andrade, E. N., and R. F. Y. Randall (1949), The Rehbinder effect, *Nature*, *164*, 1127.

Armitrano, D., and A. Helmstetter (2006), Brittle creep, damage, time to failure in rocks, *J. Geophys. Res.*, *111*, B11201, doi:10.1029/2005JB004252.

Atkinson, B. K. (1979), A fracture mechanics study of subcritical tensile cracking of quartz in wet environments, *Pure Appl. Geophys.*, *117*, 1011–1024.

Atkinson, B. K. (1984), Subcritical crack growth in geological materials, *J. Geophys. Res.*, *89*, 4077–4114.

Atkinson, B. K., and P. G. Meredith (1981), Stress corrosion cracking of quartz: A note on the influence of chemical environment, *Tectonophysics*, *77*, 1–11.

Atkinson, B. K., and P. G. Meredith (1987), The theory of subcritical crack growth with applications to minerals and rocks, in *Fracture Mechanics of Rock*, edited by B. K. Atkinson, pp. 111–166, Academic Press, London, U. K.

Baud, P., and P. G. Meredith (1997), Damage accumulation during triaxial creep of Darley Dale sandstone from pore volumometry and acoustic emission, *Int. J. Rock Mech. Min. Sci.*, *34*, 024.

Baud, P., W. Zhu, and T.-F. Wong (2000), Failure mode and weakening effect of water on sandstone, *J. Geophys. Res.*, *105*, 16,371–16,389.

Benson, P. M., A. B. Thompson, P. G. Meredith, S. Vinciguerra, and R. P. Young (2007), Imaging slow failure in triaxially deformed Etna basalt using 3D acoustic-emission location and X-ray computed tomography, *Geophys. Res. Lett.*, *34*, L03303, doi:10.1029/2006GL028721.

Byerlee, J. (1967), Frictional characteristics of granite under high confining pressure, *J. Geophys. Res.*, *72*, 3639–3648.

Charles, R. J. (1958), Static fatigue of glass, *J. Appl. Phys.*, *29*, 1549–1560.

Charles, R. J., and W. B. Hillig (1962), The kinetics of glass failure by stress corrosion, in *Symposium sur la resistance mechanique du verre et les moyens de l'ameliorer*, Rue Dourler, Charleroi, Belgium.

Cornelius, R. R., and P. A. Scott (1993), A materials failure relation of accelerating creep as empirical description of damage accumulation, *Rock Mech. Rock Eng.*, *26*(3), 233–252.

Costin, (1987), Time-dependent deformation and failure, in *Fracture Mechanics of Rock*, edited by B. K. Atkinson, pp. 167–216, Academic Press, London, U. K.

Cox, S. J. D., and P. G. Meredith (1993), Microcrack formation and material softening in rock measured by monitoring acoustic emissions, *Int. J. Rock Mech. Min. Sci. Geomech. Abstr.*, *30*, 11–24.

Crampin, S., R. Evans, and B. K. Atkinson (1984), Earthquake prediction: A new physical basis, *Geophys. J. Int.*, *76*, 147–156.

Cruden, D. M. (1974), Static fatigue of brittle rock under uniaxial compression, *Int. J. Rock Mech. Min. Sci.*, *11*, 67–73.

Das, S., and C. H. Scholz (1981), Theory of time-dependent rupture in the Earth, *J. Geophys. Res.*, *86*, 6039–6051.

Diederichs, M. S., and P. K. Kaiser (1999), Tensile strength and abutment relaxation as failure control mechanisms in underground excavations, *Int. J. Rock Mech. Min. Sci.*, *36*, 69–96.

Fortin, J., S. Stanchits, G. Dresen, and Y. Gueguen (2006), Acoustic emission and velocities associated with the formation of compaction bands in sandstone, *J. Geophys. Res.*, *111*, B10203, doi:10.1029/2005JB003854.

Francois, D., and T. R. Wilshaw (1968), The effect of hydrostatic pressure on the cleavage fracture of polycrystalline materials, *J. Appl. Phys.*, *39*, doi:10.1063/1.1656943.

Freiman, S. W (1984), Effects of the chemical environment on slow crack growth in glasses and ceramics, *J. Geophys. Res.*, *89*, 4072–4076.

Fyfe, W. S., N. J. Price, and A. B. Thompson (1978), *Fluids in the Earth's Crust*, Elsevier, Amsterdam.

Griggs, D. (1939), Creep of rocks, *J. Geol.*, *47*, 225–251.

Griggs, D. (1940), Experimental flow of rocks under conditions favoring recrystallization, *Bull. Seismol. Soc. Am.*, *51*, 1001–1022.

Hadizadeh, J., and R. D. Law (1991), Water-weakening of sandstone and quartzite deformed at various stress and strain rates, *Int. J. Rock Mech. Min. Sci. Geomech. Abstr.*, *28*, 431–439.

Hawkes, I., and M. Mellor (1970), Uniaxial testing in rock mechanics laboratories, *Eng. Geol.*, *4*, 177–285.

Hillig, W. B., and R. J. Charles (1965), Surfaces, stress-dependent reactions, and strength, in *High Strength Materials*, edited by V. F. Zackay, pp. 682–705, Wiley, New York.

Hirata, T., T. Satoh, and K. Ito (1987), Fractal structure of spatial distribution of microfracturing in rock, *Geophys. J. Int.*, *90*, 369–374.

Jaeger, J., N. G. W. Cook, and R. Zimmerman (2007), *Fundamentals in Rock Mechanics*, 4th ed., Blackwell Publ., London, U. K.

Kilburn, C. R. J. (2003), Multiscale fracturing as a key to forecasting volcanic eruptions, *J. Vol. Geotherm. Res.*, *125*, 271–289.

Kilburn, C. R. J., and B. Voight (1998), Slow rock fracture as eruption precursor at Soufriere Hills volcano, Montserrat, *Geophys. Res. Lett.*, *25*, 3665–3668.

Kranz, R. (1980), The effect of confining pressure and stress difference on static fatigue of granite, *J. Geophys. Res.*, *85*, 1854–1866.

Kranz, R., and C. H. Scholz (1977), Critical dilatant volume of rocks at the onset of tertiary creep, *J. Geophys. Res.*, *82*, 4893–4898.

Kranz, R., W. J. Harris, and N. L. Carter (1982), Static fatigue of granite at 200°C, *Geophys. Res. Lett.*, *9*, 1–4.

Lawn, B. (1993), *Fracture of Brittle Solids*, Cambridge Univ. Press, Cambridge, U. K.

Lei, X., K. Kusunose, M. V. M. S. Rao, O. Nishizawa, and T. Satoh (2000), Quasi-static fault growth and cracking in homogeneous brittle rock under triaxial compression using acoustic emission monitoring, *J. Geophys. Res.*, *105*, 6127–6139.

Lei, X., K. Masuda, O. Nishizawa, L. Jouniaux, L. Liu, W. Ma, T. Satoh, and K. Kusunose (2004), Detailed analysis of acoustic emission activity during catastrophic fracture of faults in rock, *J. Struct. Geol.*, *26*, 247–258.

Lockner, D. (1993a), The role of acoustic emission in the study of rock fracture, *Int. J. Rock Mech. Min. Sci. Geomech. Abstr.*, *30*, 883–889.

Lockner, D. (1993b), Room temperature creep in saturated granite, *J. Geophys. Res.*, *98*, 475–487.

Lockner, D. (1998), A generalized law for brittle deformation of Westerly granite, *J. Geophys. Res.*, *103*, 5107–5123.

Lockner, D., and J. Byerlee (1975), Acoustic emission and creep in rock at high confining pressure and differential stress, *Bull. Seismol. Soc. Am.*, *67*, 247–258.

Lockner, D., and J. Byerlee (1992), Fault growth and acoustic emissions in confined granite, *Appl. Mech. Rev.*, *45*, 165–173.

Lockner, D., J. Byerlee, V. Kuksenko, A. Ponomarev, and A. Sidorin (1991), Quasi-static fault growth and shear fracture energy in granite, *Nature*, *350*, 39–42.

Lockner, D., J. Byerlee, V. Kuksenko, A. Ponomarev, and A. Sidorin (1992), Observations of quasistatic fault growth from acoustic emissions, in *Fault Mechanics and Transport Properties in Rock*, edited by J. R. Rice, B. Evans, and T.-F. Wong, pp. 3–31, Academic Press, London.

Main, I. G. (1999), Applicability of time-to-failure analysis to accelerated strain before earthquakes and volcanic eruptions, *Geophys. J. Int.*, *139*, F1–F6.

Main, I. G. (2000), A damage mechanics model for power-law creep and earthquake aftershock and foreshock sequences, *Geophys. J. Int.*, *142*, 151–161.

Main, I. G., and P. G. Meredith (1991), Stress corrosion constitutive laws as a possible mechanism of intermediate-term and short-term seismic quiescence, *Geophys. J. Int.*, *107*, 363–372.

Main, I. G., P. G. Meredith, and P. R. Sammonds (1992), Temporal variations in seismic event rate and b-values from stress corrosion constitutive laws, *Tectonophysics*, *211*, 233–246.

Main, I. G., P. R. Sammonds, and P. G. Meredith (1993), Application of a modified Griffith criterion to the evolution of fractal damage during compressional rock failure, *Geophys. J. Int.*, *115*, 367–380.

Maranini, E., and M. Brignoli (1999), Creep behavior of a weak rock: Experimental characterization, *Int. J. Rock Mech. Min. Sci.*, *36*, 127–138.

McGuire, W. J., and C. R. J. Kilburn (1997), Forecasting volcanic events: Some contemporary issues, *Geol. Rundsch.*, *86*, 439–445.

Meredith, P. G., and B. K. Atkinson (1982), High-temperature tensile crack propagation in quartz: Experimental results and application to time-dependent earthquake rupture, *Earthquake Predict. Res.*, *1*, 377–391.

Meredith, P. G., and B. K. Atkinson (1983), Stress corrosion and acoustic emission during tensile crack propagation in Whin Sill dolerite and other basic rocks, *Geophys. J. Int.*, *75*, 1–21.

Meredith, P. G., and B. K. Atkinson (1985), Fracture toughness and subcritical crack growth during high-temperature tensile deformation of Westerly granite and Black gabbro, *Phys. Earth Planet. Int.*, *39*, 33–51.

Michalske, T. A., and S. W. Freiman (1982), A molecular interpretation of stress corrosion in silica, *Nature*, *295*, 511–512.

Michalske, T. A., and S. W. Freiman (1983), A molecular mechanism for stress corrosion in vitreous silica, *J. Am. Ceram. Soc.*, *66*, 284–288.

Mogi, K. (1966), Some precise measurements of fracture strength of rocks under uniform compressive stress, *Rock Mech. Eng. Geol.*, *4*, 41–55.

Ngwenya, B. T., I. G. Main, S. C. Elphick, B. R. Crawford, and B. G. D. Smart (2001), A constitutive law for low-temperature creep of water-saturated sandstones, *J. Geophys. Res.*, *106*, 21,811–21,826.

Nishizawa, O., and H. Noro (1990), Self-exciting process of acoustic emission occurrence in steady creep of granite under uniaxial stress, *Geophys. Res. Lett.*, *17*, 1521–1524.

Nishizawa, O., K. Onai, and K. Kusunose (1984), Hypocenter distribution and focal mechanism of AE events during two stress stage creep in Yugawara andesite, *Pure Appl. Geophys.*, *122*, 36–52.

Ohnaka, M. (1973), The quantitative effect of hydrostatic confining pressure on the compressive strength of crystalline rocks, *J. Phys. Earth*, *21*, 125–140.

Ohnaka, M. (1983), Acoustic emission during creep of brittle rock, *Int. J. Rock Mech. Min. Sci. Geomech. Abstr.*, *20*, 121–134.

Ojala, I. O., B. T. Ngwenya, I. G. Main, and S. C. Elphick (2003), Correlation of microseismic and chemical properties of brittle deformation in Locharbriggs sandstone, *J. Geophys. Res.*, *108*(B5), 2268, doi:10.1029/2002JB002277.

Olson, J. E. (1993), Joint pattern development: Effects of subcritical crack growth and mechanical crack interaction, *J. Geophys. Res.*, *98*, 12,251–12,265.

Orowan, E. (1944), The fatigue of glass under stress, *Nature*, *154*, 341–343.

Paterson, M. S. (1958), Experimental deformation and faulting in Wombeyan marble, *Bull. Seismol. Soc. Am.*, *69*, 465–475.

Paterson, M. S., and T.-F. Wong (2005), *Experimental Rock Deformation — The Brittle Field*, Springer, New York.

Rehbinder, P. A. (1948), *Hardness Reducers in Drilling* (translated from Russian), CSIR, Melbourne, Australia.

Renshaw, C. E., and D. D. Pollard (1994), Numerical simulation of fracture set formation: A fracture mechanics model consistent with experimental observations, *J. Geophys. Res.*, *99*, 9359–9372.

Rummel, F., and C. Fairhurst (1970), Determination of the post-failure behavior of brittle rock using a servo-controlled testing machine, *Rock Mech. Rock Eng.*, *2*, 189–204.

Rutter, E. H., and D. H. Mainprice (1978), The effect of water on stress relaxation of faulted and unfaulted sandstone, *Pure Appl. Geophys.*, *116*, 634–654.

Sammonds, P. R., P. G. Meredith, and I. G. Main (1992), Role of pore fluids in the generation of seismic precursors to shear fracture, *Nature*, *359*, 228–230.

Savalli, L., and T. Engelder (2005), Mechanisms controlling rupture shape during subcritical growth of joints in layered rocks, *GSA Bull.*, *117*, 436–449.

Scholz, C. H. (1968a), The frequency-magnitude relation of microfracturing in rock and its relation to earthquakes, *Bull. Seismol. Soc. Am.*, *58*, 399–415.

Scholz, C. H. (1968b), Microfractures, aftershocks, and seismicity, *Bull. Seismol. Soc. Am.*, *58*, 1117–1130.

Stanchits, S., S. Vinciguerra, and G. Dresen (2006), Ultrasonic velocities, acoustic emission characteristics and crack damage of basalt and granite, *Pure Appl. Geophys.*, *163*, 975–994.

Swanson, P. L. (1984), Subcritical crack growth and other time- and environment-dependent behavior in crustal rocks, *J. Geophys. Res.*, *89*, 4137–4152.

Terzaghi, K. (1943), *Theoretical Soil Mechanics*, Wiley, New York.

Thompson, B. D., R. P. Young, and D. Lockner (2006), Fracture in Westerly Granite under AE feedback and constant strain rate loading: Nucleation, quasi-static propagation, and the transition to unstable fracture propagation, *Pure Appl. Geophys.*, *163*, 995–1019.

Townend, E., B. D. Thompson, P. M. Benson, P. G. Meredith, P. Baud, and R. P. Young (2008), Imaging compaction band propagation in Diemelstadt sandstone using acoustic emission locations, *Geophys. Res. Lett.*, *35*, L15301, doi:10.1029/2008GL034723.

Underwood, E. E. (1970), *Quantitative Stereology*, Addison Wesley, Reading, Mass.

Voight, B. (1988), A method for prediction of volcanic eruptions, *Nature*, *332*, 125–130.

Voight, B. (1989), A relation to describe rate-dependent material failure, *Science*, *243*, 200–203.

Wawersik, W. R., and W. F. Brace (1971), Post-failure behavior of a granite and diabase, *Rock Mech. Rock Eng.*, *3*, 61–85.

Wawersik, W. R., and W. S. Brown (1973), Creep fracture in rock, *Utah University Salt Lake City Department of Mechanical Enginnering*, *Final report UTEC-ME-73-197*, 28 December–28 July, Defense Technical Information Center, Vancouver, Canada.

Wiederhorn, S. M., and L. H. Bolz (1970), Stress corrosion and static fatigue of glass, *J. Am. Ceram. Soc.*, *53*, 543–548.

Wong, T.-F., C. David, and W. Zhu (1997), The transition from brittle faulting to cataclastic flow in porous sandstones: Mechanical deformation, *J. Geophys. Res.*, *102*, 3009–3025.

Wu, F. J., and L. Thomsen (1975), Microfracturing and deformation of Westerly granite under creep condition, *Int. J. Rock Mech. Min. Sci. Geomech. Abstr., Abst.*, *12*, 167–173.

Wu, X. Y., P. Baud, and T.-F. Wong (2000), Micromechanics of compressive failure and spatial evolution of anisotropic damage in Darley Dale sandstone, *Int. J. Rock Mech. Min. Sci.*, *37*, 143–160.

Yanagidani, T., S. Ehara, O. Nishizawa, K. Kusunose, and M. Terada (1985), Localization of dilatancy in Ohshima granite under constant uniaxial stress, *J. Geophys. Res.*, *90*, 6840–6858.

Zang, A., F. C. Wagner, and G. Dresen (1996), Acoustic emission, microstructure, and damage model of dry and wet sandstone stressed to failure, *J. Geophys. Res.*, *101*, 17,507–17,521.

Zhu, W., and T.-F. Wong (1997), The transition from brittle faulting to cataclastic flow: Permeability evolution, *J. Geophys. Res.*, *102*, 3027–3041.

P. Baud, EOST, CNRS/ULP, 5 rue René Descartes, Strasbourg, France.

A. F. Bell and I. G. Main, School of GeoSciences, University of Edinburgh, Grant Institute, The King's Buildings, West Mains Road, Edinburgh EH9 3JW, UK.

M. J. Heap and P. G. Meredith, Rock and Ice Physics Laboratory, Department of Earth Sciences, University College London, Gower Street, London WC1E 6BT, UK. (m.heap@ucl.ac.uk)